POLITECNICO DI MILANO

Master Degree in Materials Engineering and Nanotechnology
School of Industrial and Information Engineering

FABRICATION AND CHARACTERIZATION OF COPPER SELENIDE BASED NANOCOMPOSITES FOR THERMOELECTRIC APPLICATIONS

Politecnico di Milano - Department of Energy
Micro and Nanostructured Materials Group

KTH - Royal Institute of Technology - Department of Materials and Nanophysics
Functional Materials Division

Internal Supervisor: Professor Carlo E. Bottani
External Supervisors: Professor Muhammet S. Toprak
Doctor Mohsin Saleemi

Master Thesis of:
Lorenzo Vinciguerra, 837194

Academic Year 2015-2016

Ai miei genitori,
per avermi sempre incoraggiato e sostenuto...

Acknowledgements

I would first like to thank Professor M. S. Toprak for giving me the opportunity of conducting research in the Functional Materials Department. He has boosted my confidence by always allowing a high degree of independence in my research while always being present for discussion when his precious help and opinions were needed. I will never be able to thank Doctor M. Saleemi enough for everything he did for me. He guided my first steps during this project and later on he has always been present to give me good advice and share his knowledge.

I would also like to acknowledge Professor C. E. Bottani for being the internal supervisor for this thesis, without his help and review this document would not have been possible.

A special thanks goes to everyone that helped me during these months, in particular the PhD students and researchers who spent time and patience to pass on their expertise to me and the fellow students at ICT with whom a climate of mutual help was always possible.

Finally my deepest gratitude goes to my friends, new and old, for always being there for me when I most needed them.

Abstract

Thermoelectric (TE) materials can be straightforwardly defined as materials that have a strong coupling between electronic and thermal transport: when subject to a temperature gradient they will generate a potential difference between their cold and hot side, while it is also possible to drive heat from one side to the other by drawing electric power. These features can be exploited in heat-flow related products, such as local cooling and energy harvesting, but has been up to now limited to niche applications due to high cost of TE devices and limited availability of raw materials used. Copper Selenide based TE materials have gained more and more popularity due to their relatively low cost, large availability of raw materials and high figure of merit (zT) at medium-high temperatures. Many production processes, though, revolve around time consuming and expensive top-down procedures, a common example is bulk alloying followed by ball-milling, thus outweighing the lower price advantage of said raw materials. The process proposed is instead based on microwave assisted thermolysis, an inherently bottom-up route. The precursors are dissolved in a Trioctylphosphine, Oleic Acid and 1-Octadecene solution and then heated up to the required temperature by use of microwave irradiation. The synthesis is carried out at various temperatures and following different mixing procedures in order to optimize the phase distributions obtained. The finalized processing allows compositional and crystallographic control, furthermore it also shows promise for industrial scalability. The powders produced present nanoscale dimensionality ranging from an average of 60nm to 300 nm and are used for the production of bulk nanostructured and nanocomposite materials. The particles are compacted by Spark Plasma Sintering (SPS) and preserve nano-features after this step. Details of microstructure and crystallinity are studied previous to and after SPS process. Further analysis on electrical properties are carried out on the sintered samples, showing in particular how compositing can significantly improve the Power Factor of TEs and giving interesting insights into the phase interaction mechanisms.

Sommario

I materiali termoelettrici (TE) sono caratterizzati da una forte interconnessione tra il trasporto elettronico e di calore. Nei materiali che si possono incontrare nella vita di tutti i giorni queste interazioni sono trascurabili ma, per particolari composizioni, esse diventano significative e possono essere di conseguenza sfruttate in numerose applicazioni. Il presente elaborato di tesi si focalizza su una particolare famiglia: le leghe di rame e selenio, composti definiti genericamente seleniuri di rame. Questi sono materiali semiconduttori con spiccate proprietà termoelettriche e, recentemente, grande attenzione è stata loro dedicata a seguito di studi riportanti valori del coefficiente di merito (zT) ben oltre l'unità. Questo li renderebbe interessanti candidati per la produzione di moduli per il recupero di calore da fonti quali gas di scarico nel settore automobilistico ed industriale, ma anche per impianti ibridi per la produzione di energia elettrica, soprattutto considerando la facile reperibilità ed il costo relativamente basso dei materiali di partenza. In questo studio si propongono i reattori a microonde come valida alternativa per la loro produzione, andando a sostituire metodi basati su processi lenti ed energivori, quali la fusione e successiva macinazione di lingotti. Le nano-polveri di seleniuro di rame sono in questo caso ottenute tramite una reazione di termolisi assistita da microonde, partendo dai seguenti reagenti: acetato di rame, polvere di selenio, acido oleico e trioctilfosfina dispersi in 1-ottadecene. In questo documento è illustrata l'ottimizzazione dei parametri di reazione, essa ha portato ad ottenere due fasi distinte:

- $Cu_{1.8}Se$
- Cu_2Se

Queste sono caratterizzate strutturalmente e dal punto di vista della composizione tramite diffrazione a raggi X (XRD), microscopia a scansione elettronica (SEM), calorimetria differenziale a scansione (DSDC) e spettroscopia di emissione atomica (ICPAES). Una volta confermato che le polveri pre-

sentino le caratteristiche desiderate, l'attenzione si sposta sulla produzione di nano-compositi, utilizzando le due fasi prodotte. Per la compattazione delle polveri si ricorre allo "spark plasma sintering", ossia la sinterizzazione assistita da plasma. Le varie composizioni utilizzate richiedono l'ottimizzazione dei parametri di sinterizzazione e al termine di questa, è reso possibile l'ottenimento di pellet, la cui struttura e composizione sono caratterizzate tramite XRD, SEM e spettroscopia EDX. Il livello di densificazione ottenuto è inoltre verificato tramite il principio di Archimede e confrontato con la densità dei rispettivi materiali "bulk". Una volta ottenuto un processo di produzione ripetibile e affidabile ed avendo verificato la validità dei parametri finali, le proprietà di trasporto elettrico e termico dei materiali ottenuti sono misurate e da esse il coefficiente di merito zT può essere ricavato.

Contents

List of Figures

List of Tables

Chapter 1

Introduction

1.1 Current Energy Situation

In a world where energy consumption is growing continuously great attention is devoted towards the improvement of systems efficiency. Although even greater emphasis is put on increasing the use of renewable energy sources, a quick data survey shows that use of fossil fuels is not going down but has actually increased significantly in the last 10 years.

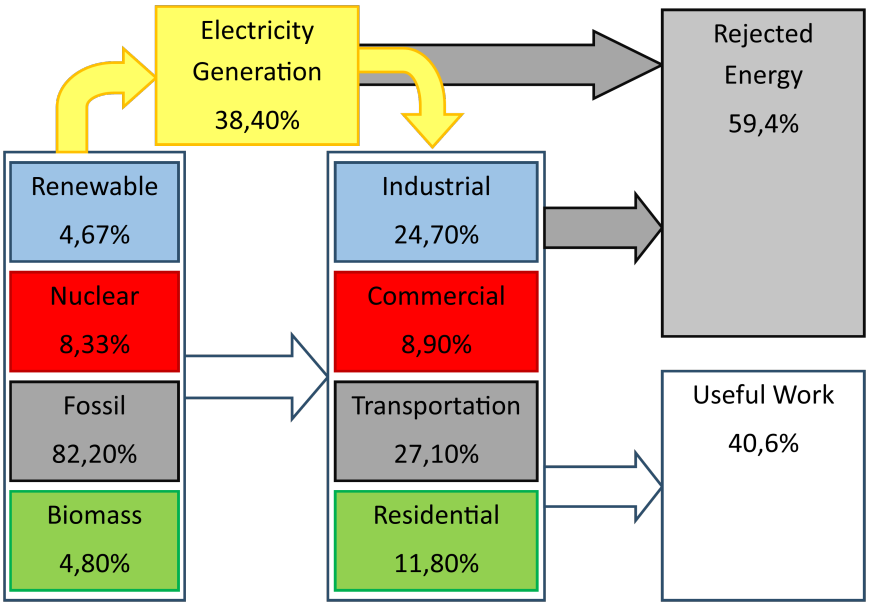

Figure 1.1: Adapted from U.S.A. Energy Flow Chart 2014 by Lawrence Livermore National Laboratory [32]

Society is, therefore, still very far from being able to discard fossil fuels as

energy sources and a realistic approach should concentrate on obtaining as much useful work as possible from them. An interesting analysis can be obtained from energy flow charts. In Figure 1.1 from 2014 we can easily see that more than 80% of the energy used in the U.S.A. still comes from fossil fuels, but an even more striking data is the Rejected Energy count. We can see that almost 60% of the energy consumed is not put to useful work but is lost in the process. Quantifying how much of this energy could be recovered is not an easy task, however, considering that almost 90% of the primary energy is transformed to heat before being converted to useful work, [10] something can and must be done.
Thermoelectric (TE) materials can play a role in this challenging field and, although it is obvious that they cannot solve the problem alone, even comparably small efficiency improvements can make a difference. In particular, these materials can have the biggest impact in power plants and transportation, fields that are still only 25 to 32% efficient. An example of application could be in cars, where 30% of the energy is lost as heat in the exhaust gases, there are some complications due to temperature oscillations that must still be solved, though. An easier implementation might be, instead, topping cycles in coal and gas powered plants. The efficiency of steam turbines, in particular, is limited by the maximum operating temperature and this gap can be filled by inserting a TE conversion module between the flame and the working fluid. Using the graphs reported in Figures 1.2 and 1.3 and optimization algorithms it is possible to estimate an increase of 2.6% to 8.2% in the overall cycle efficiency employing materials with zT values from 0.3 to 1; these are representative figures of merit already achievable with current technology, and their precise meaning is clarified in subsequent sections. Overall, it is possible to conclude that TE materials could play a role in better energy extraction from conventional sources by recovering heat that would otherwise be lost; their implementation could therefore be a fairly straightforward route for improving current systems efficiency with the added advantage of requiring minor modifications to existing power plants. This projection comes with challenges as well: before industrial application, competitive production processes must be developed for these materials and overall stability and lifetime of the devices must be further studied and improved.

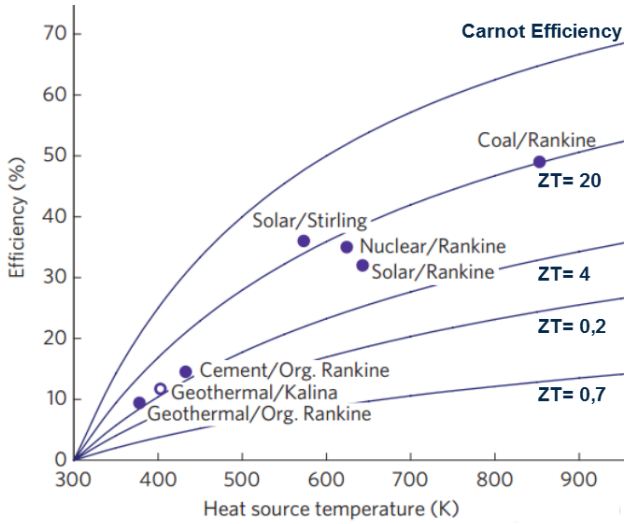

Figure 1.2: Thermoelectrics and Thermal Engines comparison (Adapted from Vining [48])

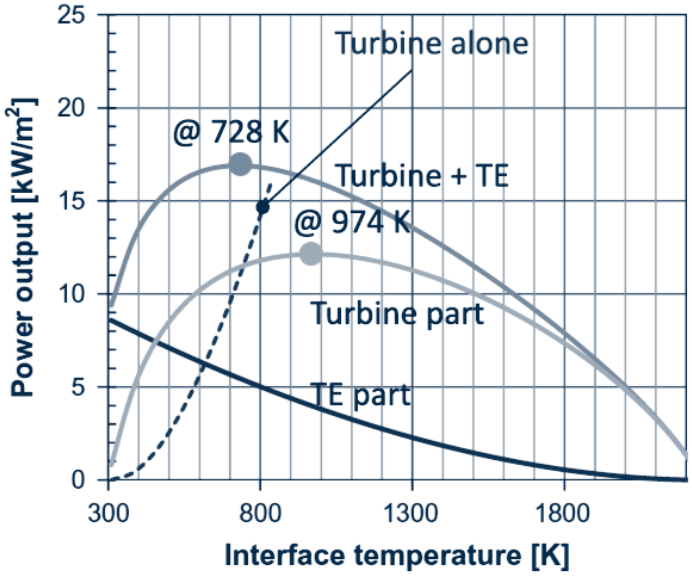

Figure 1.3: Thermoelectrics and Thermal Engines coupling graph showing power outputs of: Steam turbine alone, steam turbine coupled with a TE module and the individual contributions of steam turbine and TE module in the combined system (Adapted from Yazawa et al. [56])

1.2 Thermoelectric Materials

1.2.1 History

The TE effect was first noticed by Thomas Johann Seebeck in the early 1800s while experimenting with two metal-metal junctions kept at different temperatures. He noticed that the circuit created would deflect a compass needle and, after further studies, was able to connect this effect to the current generated in the circuit.

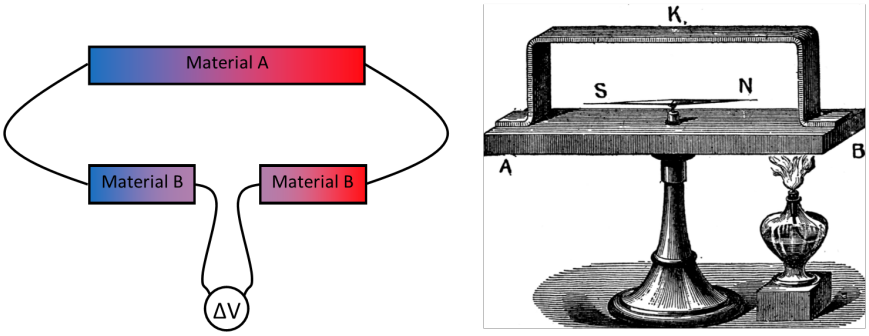

Figure 1.4: Schematic of Seebeck Effect and the first experiment.

The circulation of current is in turn caused by an electric potential that is proportional to the temperature difference between the two junctions. The ratio of voltage generated and temperature difference is named Seebeck coefficient and is an intrinsic property of the couple of materials utilized. A related effect was discovered only a few years later by Jean Charles Athanase Peltier, in this case a current is forced through a junction of two different metals and either heating or cooling occurs depending on the current direction. The coefficient relating the applied current and the heat transported is named after the French physicist and is bound to the Seebeck coefficient by a very simple relationship:

$$\Pi = S \cdot T \tag{1.1}$$

Where Π is the Peltier coefficient, S the Seebeck coefficient and T the absolute temperature. This relationship was formulated by William Thomson, better known as Lord Kelvin, only 20 years after the first observation of the Peltier Effect. During his studies the English scientist actually discovered a second effect named after him: the Thomson Effect. In this particular phenomenon heat is produced or absorbed when a current circulates in a material subject to a temperature gradient, once again this is only another

manifestation of the same underlying physical phenomenon: thermoelectricity. These discoveries catalysed great interest already in those years, when the main focus was increasing the knowledge of the so called "electric fluid". Particularly interesting for this thesis work is the case of Antoine César Becquerel; this French scientist was experimenting with platinum and copper rings heated by candles when he noticed that the measured currents where significantly higher in copper wires with sulphur powder melted on top. This episode dates 1827 and can be considered one of the first documented cases of Copper Sulphides as TE material, although obtained by pure chance. The studies on sulphides continued with Becquerel son, Alexandre Edmond Becquerel who measured for the first time the performances of Cu-Ni-Zn and Copper Sulfide, further obtaining a rudimental device by coupling the two materials.[12] A more application focused study of TE materials was performed by Edmund Altenkirch in the first years of the 20^{th} century. He was the first to derive the maximum theoretical efficiency of a TE generator in 1909 and that of cooler in 1911. His pragmatic approach to the subject led him to lay the foundations of TE performance estimation: the dimensionless figure of merit zT.

$$zT = \frac{\sigma \cdot S^2 \cdot T}{k} \tag{1.2}$$

Where σ is the electrical conductivity, S the Seebeck coefficient and k the thermal conductivity. More in details explanations on the meaning of this coefficient are given in Section 1.3.3 but for the moment it is sufficient to know that it is still widely used today, more than 100 years later, to rapidly compare materials in their operating temperature ranges. Still in the beginning of the 20^{th} century another important contribution came from the research on lattice thermal conductivity performed by Arnold Eucken, who mainly concentrated on its reduction caused by the presence of lattice defects. As shown in later sections, this is still one of the main strategies for improving the performance of TE materials and thanks to the manipulation of the crystal it is possible to have striking effects on the scattering of phonons. Nonetheless, the real boom in application-focused studies took place during and after the World Wars, in this period efficiencies of over 5% were achieved and TE materials were meant to substitute conventional heat engines in the near future. This proved a very optimistic prediction since, already in the 1960s the efficiency improvement had significantly slowed down, up to a stand-still, when values of zT of around 1 were achieved in numerous studies. The consequent distrust in the future of this technology led to many research programs being dismantled and only in the 1970s new niche applications arose that would allow a revival of TE materials. In particular, the

field of optoelectronics, micro-refrigeration and aerospace industry asked for miniaturized, lightweight and reliable solutions for heat transfer and power generation. In situations where the high fabrication cost was not an issue, TE materials could provide alternative solutions to these challenges and a number of scientific meeting and joint research projects were issued during those years. TE devices were, therefore, segregated to very specialized applications and the number of available literature was reduced by the need for secrecy, particularly in the aerospace field. Only in the early 2000s the studies of Dresselhaus on the effects of nanostructuring [13] created a new trend in TE research; the new focus is obtaining inexpensive and environmentally friendly materials that can provide sufficiently high performances in consumer oriented applications, like topping cycles and waste heat recovery. More specific information on the present trends and future perspectives are presented in the following sections.

1.2.2 Applications

Many fields have benefited from the discoveries in the field of thermoelectricity and multiple applications can be opened by improvement of zT and a lowering of the cost of fabrication.

Cooling Devices

A very interesting possibility explored both by independent researchers and large IT companies is the fabrication of devices to reduce local overheating in microprocessors. The continuous rise in power density of the integrated circuits (Fig. 1.5) is not followed at sufficient speed by the improvements in traditional cooling systems. While the passive cooling systems are ill suited to compensating sudden spikes in temperature, this is becoming a very common issue, particularly in portable devices where high computing power is harvested in short bursts to reduce energy consumption. It has been demonstrated that every 10°C increase in junction temperature can reduce the life expectancy of components by a factor of two. [33] TE active cooling systems could be a solution, they could accumulate waste heat energy in form of electricity when the CPU is running idle and exploit it for cooling during high demanding operations, when the passive system is not able to achieve sufficient heat removal. [11] [2] An application that has been already implemented, but could still be improved, is active cooling of sensors to reduce the thermal noise, this is particularly appealing in the case of X-ray detectors for astronomy. [3] It has been demonstrated that a simple device with max power requirement of 3W is able to stabilize the sensor's tempera-

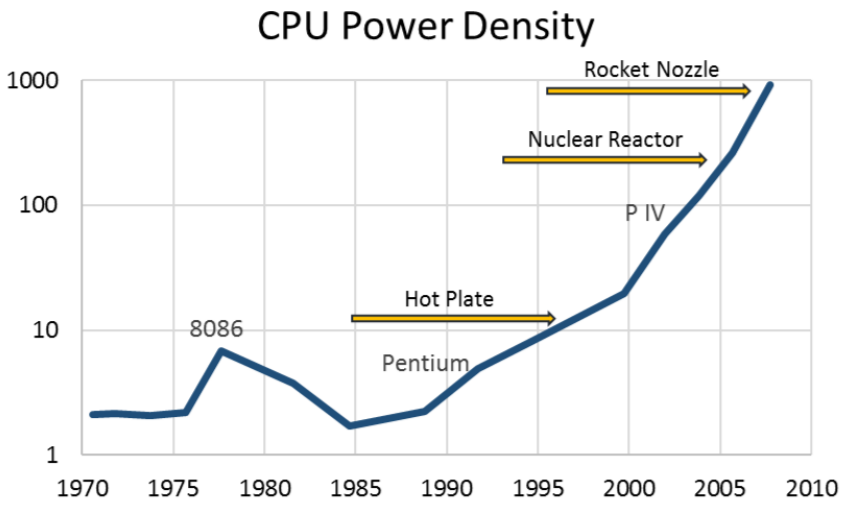

Figure 1.5: Increase in CPUs power density over recent years, (Adapted from Intel [23])

ture to $-40°C$ acting between it and a $10°C$ heat sink connected to a water cooler. [39] Finally, macroscopic example of TE cooling devices are portable cooler boxes and body cooling vests for military applications. Only in these niche cases the low coefficient of performance, related to zT value, and high cost did not limit their use, but in recent years the increase in zT and the cost reduction opened the road for everyday life use. Alternatives to conventional air conditioning have been proposed, these would allow more compact systems compared to fluid compressor based ones and could also be directly coupled to photovoltaic devices reducing energy consumption during the hot season. [39] The use of TEs in everyday temperature regulation is limited to luxury car seats and driving wheels, in these cases the relatively high price is justified by the faster comfort level obtained with respect to achieving the desired temperature of these parts by traditional air conditioning. In future years, modules could be implemented to completely substitute the automotive conditioning systems with TE devices. This would have a series of advantages the most important of which are: faster cooling and heating as needed, lower weight, better temperature control and the ability of cooling or heating the passengers' bodies instead of the whole car, increasing efficiency.

Energy Harvesting

When talking about energy harvesting by TE modules it is necessary to focus on two main parameters: the running cost and the system cost. Since

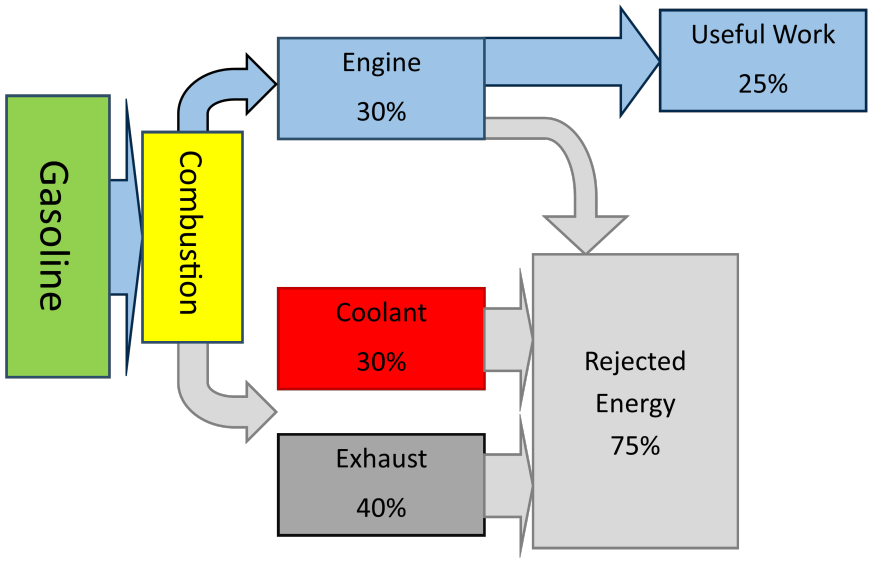

Figure 1.6: Typical car energy flow diagram (Adapted from TE automotive applications [53])

the main perspective for these materials is waste heat recovery, it is possible to consider the price of the energy source negligible and, therefore, the relatively low efficiency is less of an issue and attention can be diverted to obtaining lower cost devices. With commercially available TE materials it is already possible to obtain figures of about 4 $\$/W$ and the cost can be further reduced increasing the working temperature difference. An example of application in the automotive sector comes from BMW. [5] In 2009 Munich Motorshow, the German company presented a prototype car that integrated a TE device to recover heat from the exhaust gases. The maximum power output is 200W and the idea behind it is recovering waste energy for on-board power supply. This is only a very small step though, if we look at energy diagrams for cars the amount of heat expelled with exhaust gases accounts for more than half of the total wasted power. (Figure 1.6) [53]

A very nice possibility of exploiting the compact nature of TE modules is in co-generation plants, in this case the device is positioned at the output of a fluid heater and will convert part of the heat in electricity. Here its low efficiency is not a big issue if the main objective is production of hot fluids and electric generation comes as a second added benefit, actually the TE device can be exploited as a further temperature regulation system as well. A similar concept is that of coupling a gas turbine generator with a TE energy harvesting module, here the efficiency requirements will be higher though, and only materials with zT higher than 1 can be implemented to

increase the overall productivity of the powerplant. [55] It must be noticed that zT of 1 or more are already achievable and a large efficiency improvement step, happening between 1 and 2, is underway. It has been shown that coupling the two systems not only can increase the overall efficiency but also lowers the needed working temperature for the turbine. [55] Increasing the operating temperature has, in fact, been the main strategy to achieve higher gas turbine efficiency but materials that can sustain prolonged use in more and more demanding conditions are difficult to engineer and these coupled systems could be a valid alternative.

Sensing Devices

Thermal Energy sensing is the main field where TE devices can have an edge over traditional sensing technologies. They can be used to obtain very simple systems with no moving parts, therefore allowing not only very high precision but extreme reliability and durability. An example of application are cryogenic heat flux sensors: it has been shown that Bismuth Telluride based modules, tested in the range from 200K to 60K, can achieve tenfold higher sensitivities with respect to conventional sensors. [21] A very specific possibility is the production of ultrasound intensity sensors: in recent time ultrasonic reactors have been suggested as a very interesting way of boosting reaction kinetics and a key necessity for these systems is the accurate measurement of their intensity output. A device can be realized embedding a TE module in an ultrasound absorbing medium, it would then be possible to provide extremely rapid feedback through the electric signal variations caused by the temperature changes of the medium. [40] Finally early detection of water condensation is very important for a variety of industrial processes and mist formation can be readily monitored by a Peltier effect junction: when water droplets accumulate at the junction its thermal inertia is modified, therefore its imposed thermal oscillations are altered and a real time estimation of the humidity in the ambient is possible. [47]

1.2.3 An interesting family: Copper Selenides

Since this work focuses on this particular family of TEs, it is interesting to illustrate their main characteristics, also referring to some historical flagstones. Studies on these materials first started in the 1980's with F.Akkad et al., [15] their paper compared them with the members of the Copper Sulfides family, that had already interested scientists from the beginning of the 20^{th} Century with a first patent by Hermite et al. in 1901. [14] In the 1990's, though, the research focus shifted to more complex formulations of TE ma-

terials, like inorganic clathrates and to other components of the chalcogenide family, such as Bismuth Tellurides. Only in 2012 interest was rekindled for Copper Selenides by the article of Liu et al. [31] in which the authors claimed a zT of 1.6 even in the coarse polycrystalline form produced. Now, with the help of novel Nano-structuring techniques, it appears possible to surpass their results achieving zT values as high as 2.1, as reported, among others, by Tafti et al. in 2016. [52] In order to work with these materials it is first necessary to get an insight on their nature, starting from their peculiar and rather complex phase diagram, Figure 1.7. The area of most interest is that

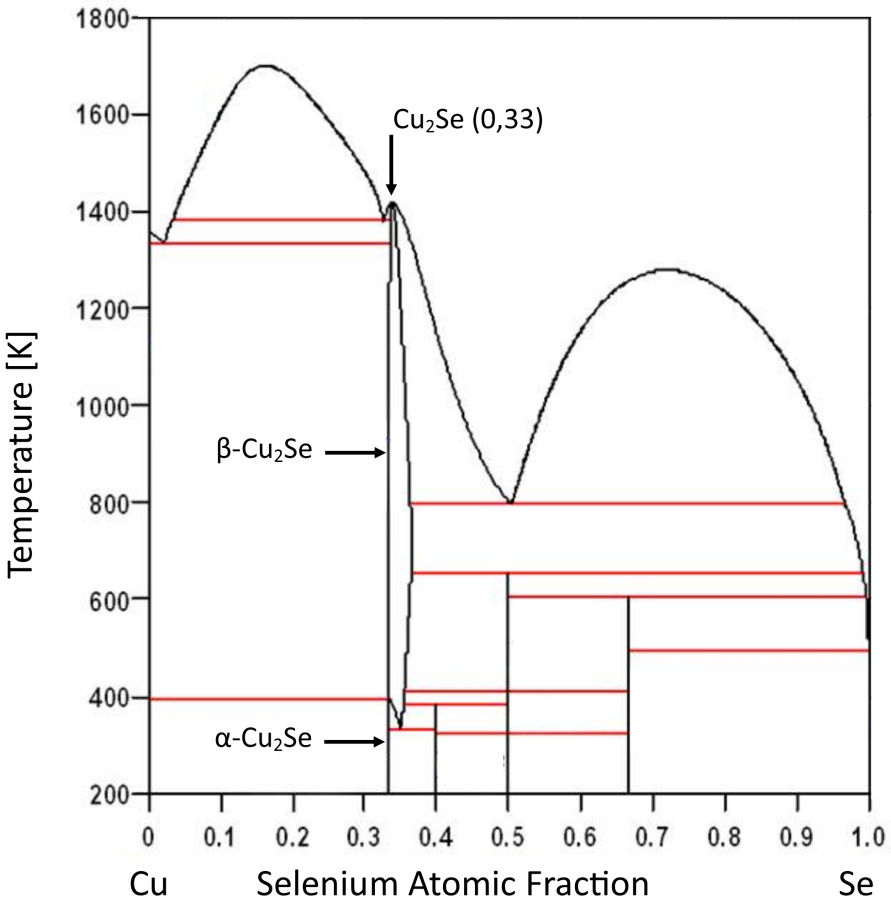

Figure 1.7: Phase Diagram of Copper-Selenium binary alloys (Adapted from Chakrabarti et al.[7])

surrounding the Cu_2Se composition, it can be noticed that this compound exists in two different forms depending on the temperature range:

- α-Cu_2Se up to 400K: a partially distorted monoclinic phase

- β-Cu_2Se from 400K up to around 800K: a face centred cubic phase, with a space group related to the common anti-fluorite. [7]

It must be made clear that these are diagrams obtained for compositions at their thermodynamic equilibrium, Copper Selenides can tolerate a very significant variation of elemental concentration without shifting to a different crystallographic shape, though. The accommodation of vacancies and defects is easily achieved through distortions of the unit cell, aspect that is also reflected in the ease with which ions can flow through the crystal. This effect, particularly evident in the β-phase, is the reason for them being named Superionic Conductors. The second interesting phase is $Cu_{1.8}Se$, this material is face centered cubic as well but with a different crystallographic space group due to the lower amount of copper ions present in each unit cell. Both Cu_2Se and $Cu_{1.8}Se$ show interesting TE properties being low band gap semiconductors, with the band gap shifting from $\approx$ 1eV to $\approx$ 0.12eV during the temperature phase transition in case of Cu_2Se [8] and being instead attested to be very low for $Cu_{1.8}Se$, this last material being claimed to even be semi-metallic at high temperatures. It is finally interesting to notice that the electrical resistivity of the two materials differs by around one order of magnitude with Cu_2Se's being measured at $1.7 \cdot 10^{-3}\Omega$cm [20] while $Cu_{1.8}Se$ shows a value of $1.42 \cdot 10^{-4}\Omega$cm at similar temperatures. [57] The very high difference in resistivity is mainly attributed to the higher concentration of carriers in $Cu_{1.8}Se$. [51] These last observations are extremely important for some of the considerations in subsequent chapters.

1.3 Fundamentals of Transport and Thermoelectricity

1.3.1 Charge Transport in Solids

The first part of this chapter focuses on the description of the electrical conduction in solids. As base for the treatment a so called "Charge Current Density Vector" is introduced that is indicated by the letter $\vec{J}$, this quantity represents the amount of charge per unit area and time flowing through a surface.

$$\vec{J} = q \cdot \langle \vec{v} \rangle \tag{1.3}$$

Where q is the unit of charge and $\langle \vec{v} \rangle$ is the average carrier speed.The resulting flux will simply be the integration of the current density vector over the total area considered:

$$\int \vec{J} \cdot \vec{n}\, dS = \vec{i} = \frac{dQ}{dT} \tag{1.4}$$

Where $\vec{n}$ is the unit vector perpendicular to the surface and dS is the infinitesimal surface area. This flux is simply the electrical current flowing through the considered surface. Remembering the local Ohm's law this expression can be easily related to conductivity of the material:

$$\vec{J} = q \cdot \langle \vec{v} \rangle = \sigma \cdot \vec{\varepsilon} \tag{1.5}$$

Where $\vec{\varepsilon}$ is the electric field and σ the material's electrical conductivity. In reality conductivity should be expressed as a matrix due to anisotropy of materials, but, for the time being, it is avoided in order to get a simpler treatment. Now that the definition for electrical current and conductivity and their relationship through electric field are set the description can continue by a classical approach, the Drude-Lorentz Model. This is based on the assumption that no collisions happen between electrons and phonons or between electrons themselves. It is therefore classified as a completely independent electron model. The only interactions that electrons have are the ones with the atomic lattice composing the crystal and they are described through a mean free path that in turn leads to the definition of a Relaxation Time (2τ). The so defined time between collisions allows to explain why the electrons are not infinitely accelerated by the applied electric field but instead travel at a speed which can be macroscopically described as constant. This average velocity is the one previously included in equation $\vec{J} = q \cdot \langle \vec{v} \rangle$. By integration of the acceleration imposed by the electric field over the mean free path the average carrier velocity is defined as:

$$\langle \vec{v} \rangle = \frac{e \cdot \vec{\varepsilon}}{m} \cdot \tau \tag{1.6}$$

Where $\vec{\varepsilon}$ is the electric field applied and m the effective mass of the charge carrier. Now, by substitution in the previous equation, the expressions for current density and conductivity is finally obtained:

$$\vec{J} = \frac{n \cdot e^2}{m} \cdot \tau \vec{\varepsilon} \tag{1.7}$$

$$\sigma = \frac{n \cdot e^2}{m} \cdot \tau \tag{1.8}$$

This classical model is incorrect from a quantum-mechanical point of view but allows the introduction of a simple theory for describing charge transport phenomena, this theory is called Kinetic Theory and is based on the Boltzmann equation. Since systems that are inherently out of equilibrium are considered, it is necessary to utilize a probability density that takes into account their tendency to relax. This is obtained by modifying the

Liouville's theorem, in it is stated that the probability density is constant along any dynamic path, but in this case it is assumed that the probability density does not remain constant, it instead changes during a characteristic relaxation time τ:

$$\frac{d\rho}{dt} = -\frac{\rho - \rho_0}{\tau} \tag{1.9}$$

Now this can be written as:

$$\frac{d\rho}{dt} = \frac{\partial\rho}{\partial t} + \frac{\partial\rho}{\partial\vec{r}} \cdot \frac{\partial\vec{r}}{\partial t} + \frac{\partial\rho}{\partial\vec{p}} \cdot \frac{\partial\vec{p}}{\partial t} = -\frac{\rho - \rho_0}{\tau} \tag{1.10}$$

Where $\vec{r}$ is the position and $\vec{p}$ the momentum. Assuming that the equilibrium perturbation causes are time independent the first term can be neglect and finally in the approximation of small perturbations the partial derivatives of the probability density can be substituted with those of the initial probability density obtaining the so called Linearized Form of Boltzmann Equation in Relaxation time.

$$\frac{d\rho}{dt} = \frac{\partial\rho_0}{\partial\vec{r}} \cdot \frac{\partial\vec{r}}{\partial t} + \frac{\partial\rho_0}{\partial\vec{p}} \cdot \frac{\partial\vec{p}}{\partial t} = -\frac{\rho - \rho_0}{\tau} \tag{1.11}$$

It must be noticed how the partial derivative with respect to time has disappeared and only the partial derivatives of space and momentum applied to the initial probability density are left. Finally, the equation is rearranged obtaining the current probability density as a function of the initial one plus a small perturbation:

$$\rho(\vec{r},\vec{p}) \approx \rho_0 - \tau \cdot \frac{\partial\rho_0}{\partial\vec{r}} \cdot \vec{v} - \tau \cdot \frac{\partial\rho_0}{\partial\vec{p}} \cdot \vec{F} \tag{1.12}$$

Where τ is the usual relaxation time dependent on momentum, v is the velocity which substitutes the time derivative of position and F is the force applied to the particle that is nothing but the time derivative of its momentum. In order for this substitution to work a semi-classical frame of reference is needed, therefore the model works better as long as only carriers close to the centre of the Brillouin Zone are considered. This also allows the exchange of the momentum dependence with the wave vector dependence through the carriers' effective mass:

$$\vec{v} = \frac{\hbar\vec{k}}{m^*} \tag{1.13}$$

$$\vec{p} = \hbar\vec{k} \tag{1.14}$$

Where $\hbar$ is the Planck constant over 2π, $\vec{k}$ is the wave vector and m^* is the carrier effective mass. Now that the starting equation of the treatment has been obtained it is possible to proceed analysing the behaviour of particles

when an external driving force is applied. In order to do so an initial probability density distribution based on the Fermi-Dirac equation is considered, this is sensible since electrons are being analysed:

$$\rho_{FD} = \frac{1}{e^{\frac{E-E_F}{k_B T}}+1} \tag{1.15}$$

And since this distribution is Temperature dependent a temperature dependence is also introduced in the Boltzmann Equation. Only conditions of time independent temperature are considered and the temperature gradients are regarded as small enough to define a Local Equilibrium. This is like saying that, although a temperature difference is present inside the crystal, it can be considered negligible at the atomic scale. Further details on the temperature effects will be given in Section 1.3.2 when considering heat transport. For the time being the temperature gradient is neglected since its effect is normally very small compared to currents caused by an externally applied electric field. At this point everything can be expressed as a function of momentum and through some mathematical passages the following expression for probability density is achieved.

$$\rho(\vec{r},\vec{k}) \approx \rho_{FD}(\vec{k}) - \tau \cdot \frac{\partial \rho_{FD}(\vec{k})}{\partial E} \cdot \vec{v}(\vec{r}) \cdot \vec{F} \tag{1.16}$$

This form is obtained by not only neglecting temperature gradient, that puts the space derivative to zero, but also by replacing the momentum derivative with the energy derivative employing the following relationship and equation 1.14.

$$\vec{v} = \frac{1}{\hbar} \cdot \frac{\partial E(\vec{k})}{\partial \vec{k}} \tag{1.17}$$

The energy derivative in equation 1.16 represents the change in carrier distribution with respect to the change in energy. At room temperature this derivative is only different from zero in a very narrow range of energies extremely close to the Fermi Energy. The Fermi Dirac distribution changes rapidly from 1 to 0 just around this energy level as can be shown by a graphical representation in Figure 1.8

It is possible, therefore, to approximate pretty accurately the derivative with a Dirac's Delta Function:

$$-\frac{\partial \rho_{FD}(\vec{k})}{\partial E} \approx \delta(E - E_F) \tag{1.18}$$

This approximation holds reasonably well for the electrons transport but is not applicable in the case of heat transport as is later shown in Section

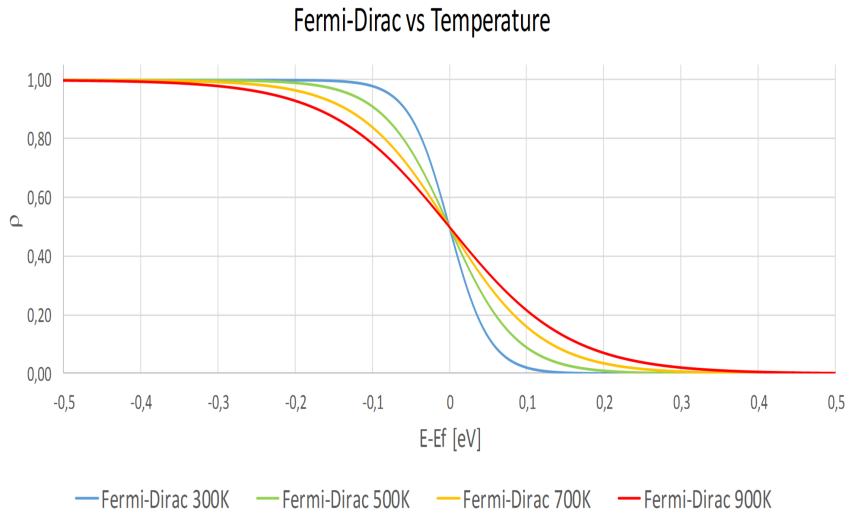

Figure 1.8: Fermi-Dirac distribution at different temperatures

1.3.2. The whole point of substituting the derivative with a delta function is obtaining an analytical expression for current density in its integral form over the possible electronic wave vectors.

$$\vec{J} = \rho(\vec{k}) \cdot \langle v \rangle = \frac{2V}{(2\pi)^3} \cdot e \cdot \int \rho(\vec{k}) \cdot \vec{v}(\vec{k}) d\vec{k} \tag{1.19}$$

As seen already, $\rho(\vec{k})$ is composed of two parts, the equilibrium distribution and the adjustment caused by perturbation. It is intuitive that the equilibrium distribution does not contribute to electricity conduction; otherwise, it would be necessary to state that currents freely circulate in materials without any external cause. Therefore, only the small out-of-equilibrium correction can be considered and substituted in equation 1.19 that, integrating over a unit volume, can be rewritten as:

$$\vec{J} = -\frac{2e}{(2\pi)^3} \cdot \int \delta\rho(\vec{k}) \cdot \vec{v}(\vec{k}) d\vec{k} \tag{1.20}$$

Referring back to equation 1.16 the following expression can be written:

$$\delta\rho(\vec{k}) = -\tau(\vec{k}) \cdot \delta(E - E_F) \cdot \vec{v}(\vec{r}) \cdot \vec{F} \tag{1.21}$$

And since the electric field is the only force externally applied to the carriers, the current becomes:

$$\vec{J} = \frac{2e^2}{(2\pi)^3} \cdot \int \tau(\vec{k}) \cdot \delta(E - E_F) \cdot [\vec{v}(\vec{k}) \cdot \vec{\varepsilon}] \cdot \vec{v}(\vec{k}) d\vec{k} \tag{1.22}$$

The part of the equation included in square brackets is a scalar product of vectors, this, in fact, would generate the conductivity of the material along the different crystallographic directions and, depending on symmetry, the components can either be all identical or require a tensor to be expressed. For the sake of simplicity this fact is ignored and attention is instead focused on the physical aspect of electron flow in a single direction. Exploiting now the properties of the Dirac's Delta a very interesting result is achieved:

$$\vec{J} = e^2 \cdot \int_{S_Ef} \tau_F \cdot \rho_{Ef}(\vec{k}) \cdot [\vec{v}(\vec{k}) \cdot \vec{\varepsilon}] \cdot \vec{v}(\vec{k}) d\vec{k} \tag{1.23}$$

It is important to spend some time analysing the obtained expression for current density, the most important and least intuitive result is the carrier density contribution to conductivity. It can be immediately noticed that only the electrons at Fermi Energy are able to conduct while all the others have no significant effect. This is derived directly from the Dirac's Delta introduced and can be partially relaxed at higher temperatures since the Fermi-Dirac distribution will become less sharp. Nevertheless, this is a minor effect and at room temperature, only minor errors are introduced by considering only electrons at exactly the Fermi Energy as available carriers. It is also noteworthy that the energy band curvature at Fermi Energy allows the prediction of which kind of carriers will be mainly responsible for conduction in the material. For example, in a metal, if the Fermi Energy encounters the branch at a negative curvature a negative effective mass is predicted, this corresponds to hole conduction, while the opposite is true for positive curvatures. Finally, it must be reminded that all effects due to temperature, defects and collisions in general are in this case included in the relaxation time at Fermi Energy (τ_F), this quantity is treated as a black box, containing all the microscopic interactions between the carriers and everything else.

1.3.2 Heat Transport in Solids

While in case of electrical conduction the definition of carriers was very straightforward in this case two cases can be distinguished:

- Heat transport in metals and good electrical conductors
- Heat transport in insulators

The main difference between the two categories is the mechanism that allows the energy transfer, in the first case the same carriers that conduct electricity are also the main responsible for heat movement while, in the second case,

since no free electrons are present, heat is carried by lattice vibrations and more specifically in energy packets called phonons. It is important to notice that, although it is impossible for insulators to have heat transfer through electrons, phonons will carry heat in conductors as well and their effect will be more or less noticeable depending on the conductivity of the materials analysed.

Electrons Heat Transport

Starting from the already stated concept of Local Thermodynamic Equilibrium this time Linear Irreversible Thermodynamics are also employed since a heat flux inherently corresponds to an entropy flux that is defined as:

$$\vec{q_S} \approx \frac{1}{T} \cdot \vec{q_u} - \frac{E_f}{T} \cdot \vec{q_n} \tag{1.24}$$

Where $\vec{q_S}$ is the entropy flux, $\vec{q_u}$ is the energy flux, $\vec{q_n}$ is simply particle flow rate and E_f is the Fermi Energy used as chemical potential substitute, since this is a good approximation in metals. Equation 1.24 is rewritten by defining the heat flux as the number of carriers multiplied by the heat they carry and their average velocity:

$$\vec{q_S} \approx \frac{1}{T} \cdot n \cdot E(\vec{k}) \cdot \vec{v}(\vec{k}) - \frac{E_f}{T} \cdot n \cdot \vec{v}(\vec{k}) \tag{1.25}$$

Now knowing that:

$$T \cdot dS = dQ \tag{1.26}$$

The equation for heat flux can be straightforwardly expressed by multiplying equation 1.25 by the temperature:

$$\vec{q_{th}} = n \cdot E(\vec{k}) \cdot \vec{v}(\vec{k}) - E_f \cdot n \cdot \vec{v}(\vec{k}) = [E(\vec{k}) - E_f] \cdot n \cdot \vec{v}(\vec{k}) \tag{1.27}$$

It is noteworthy to concentrate on the physical meaning of the equation just obtained; the electrons transport only the energy that they possess in excess of the Fermi Energy, but this means that all the electrons that have an energy close to Fermi level do not contribute to heat transfer. This creates a more complicated situation with respect to chapter 1.3.1, the Dirac's Delta is not applicable anymore to describe the energy derivative of probability density, it would, in fact, annihilate the electronic heat transfer contribution. For the time being, the integral for the computation of the number of carriers is introduced assuming that only the perturbation of the probability density distribution affects the heat transport, just like in the case of equation 1.20.

This time the transported quantity will be the energy difference between the state considered and the Fermi Energy instead:

$$\vec{q_{th}} = \frac{2}{(2\pi)^3} \cdot \int \delta\rho \cdot [E(\vec{k}) - E_f] \cdot \vec{v}(\vec{k}) dE \frac{dS_E}{|\vec{\nabla}(\vec{k})|} \tag{1.28}$$

Now assuming that no external electric field is applied the out of equilibrium density is rewritten as:

$$\delta\rho \approx \tau(\vec{k}) \cdot \vec{v}(\vec{k}) \cdot \frac{\partial \rho_{FD}}{\partial E} \cdot \frac{[E(\vec{k}) - E_f]}{T} \vec{\nabla} T \tag{1.29}$$

In this equation the effect of the temperature gradient is embedded, the change of occupation caused by the different temperatures is, in fact, what causes the movement of charge. As previously stressed, a certain range of states around the Fermi energy must be considered in order not to nullify the transport effect; an effective approximation of said interval is given by Sommerfeld and after computation the following flux equation is obtained:

$$\vec{q_{th}} = -\frac{\pi^2 k_B^2 T}{3} \cdot \int \tau(\vec{k})\ \vec{v}(\vec{k})\ \vec{v}(\vec{k})\ \rho_{Ef} dS_{Ef} \tag{1.30}$$

From the comparison with equation 1.23 a very interesting result arises: the two are strictly correlated and an increase in electrical conductivity also generates an increase in thermal conductivity for metallic behaviour. This is a very important point when discussing TE properties and allows the understanding, for example, of why metals never show high thermoelectric figures of merit. This comparison with electrical conductivity is finalised by the introduction of the Wiedemann-Franz Law. Rigorously this is only valid for metals but it can still be made to work for semi-conductors:

$$\frac{k_e}{\sigma} = LT \tag{1.31}$$

Where k_e is the thermal conductivity mediated by electrons, so defined to distinguish it from the thermal conductivity (k_L) related to phononic transport that is defined in the following section, σ is the electrical conductivity and L is the Lorentz constant that can be substituted by empirical parameters to better fit the behaviour of specific materials. In metals the thermal conductivity and electrical resistivity curves versus Temperature can be compared in order to verify that the law truly holds.

As already stated this approximation can work fairly well for degenerate semi-conductors but thermal conduction due to phonons can no longer be neglected, this transport effect is discussed in the next section.

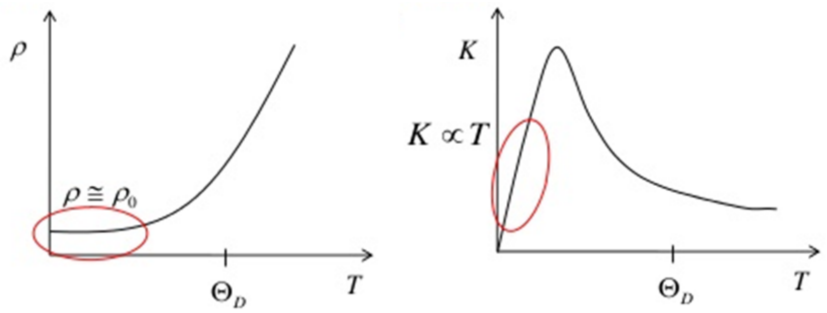

Figure 1.9: Qualitative electrical resistivity and heat conductivity vs temperature comparison (Adapted from University of Cambridge [46])

Phonons Heat Transport

In case of crystalline insulators, the electronic contribution to heat transport is obviously absent and a completely different type of carriers is considered: phonons. Phonons are defined as quasi-particles representing a collective excitation in a periodic medium. As known, they can be divided between acoustic phonons and optic phonons, but for this treatment the second ones can be neglected. This statement can be appreciated by considering their Brillouin zone band structure: as can be seen optic phonons, that are only present in poly-atomic crystals, present an extremely flat band that corresponds to very low speeds. The direct consequence is that these quasi-particles are not able to transfer energy efficiently when compared to the acoustic phonons close to the centre of the Brillouin zone.

Furthermore, even the acoustic phonons band becomes flat when moving away from Brillouin zone centre, therefore even they can be neglected in case of high wave vectors and a treatment based on long wavelength phonons is considered. In order to treat phononic transport their equilibrium distribution must be introduced, this is based on Bose-Einstein since they are bosons and therefore do not obey conservation rules:

$$\langle n(\omega)\rangle_T = \frac{1}{e^{\frac{\hbar\omega}{k_B T}} - 1} \tag{1.32}$$

From this distribution a few considerations arise, but the most significant is the fact that the lower the temperature and the lower the number of occupied states is. This directly reflects itself on the low temperature behaviour of conductivity that presents good adherence to the Debye Model while at high temperature the state distribution becomes much broader and can be approximated to:

$$\langle n(\omega)\rangle_T \approx \frac{\hbar\omega}{k_B T} \tag{1.33}$$

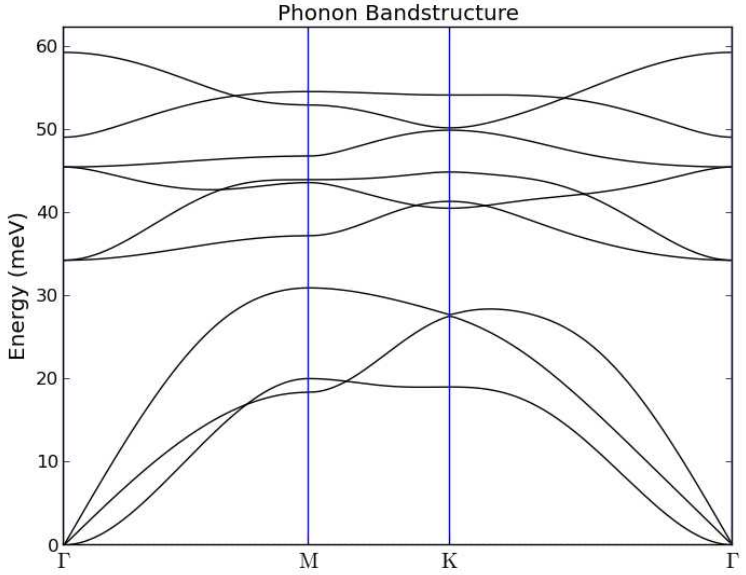

Figure 1.10: Phonons qualitative band structure (Adapted from Jiang et al.[24])

The crystal physical conditions can now be considered, a temperature gradient is introduced that is regarded as linear and constant in time for simplicity. The electric fields can be neglected if only the phononic contribution to heat transfer is analysed. Once the gradient is set the heat current density vector can be defined as:

$$q_{th} = n \cdot c \cdot v_x \frac{\Delta T}{\Delta x} \cdot x \tag{1.34}$$

Where n is the carrier density, c the heat capacity of a single carrier and v_x the speed of the carriers along the temperature gradient direction, this can be regarded as the local equivalent of macroscopic Fourier Law. As for the case of electrons, collisions effects must be introduced artificially, this is to limit the thermal conductivity, that in case of complete absence of scattering would tend to infinite. The heat current density is therefore rewritten considering a mean free path:

$$q_{th} = n \cdot c \cdot \frac{\Delta T}{\Delta x} v_x \cdot \Lambda \tag{1.35}$$

Where Λ is the mean free path of phonons. From this last expression the k_L, thermal conductivity mediated by phonons is readily deduced.

$$k_L = n \cdot c \cdot v_x \cdot \Lambda \tag{1.36}$$

At this point some of the underlying approximations must be clarified in order to be able to follow the approach: the velocity considered is that of sound in the material and is estimated to be constant with respect to temperature since its dependence on it is very subtle; the mean free path introduced is defined with an heuristic approach but is based on two types of collisions phonons can undergo:

- Phonon-defect collisions
- Phonon-phonon collisions

The modelling of these effects is quite complex and particularly for phonon-phonon interaction requires un-harmonic treatments that are well beyond the scope of this thesis work. Even without entering into too detailed physical explanations the qualitative mean free path temperature dependence can intuitively be predicted. When considering very regular structures, the mean free path is limited by defects, such as grain boundaries and impurities, only at very low temperatures, thus giving rise to almost constant Λ. Once the temperature starts to increase sufficiently the number of occupied phonon states increases, as predicted by equation 1.32, Λ therefore starts decreasing as collisions between phonons become more and more frequent. The qualitative curve can be seen in Figure 1.11, particular attention must be dedicated to the logarithmic scale used to emphasize the quasi-constant behaviour only measured at extremely low temperatures.

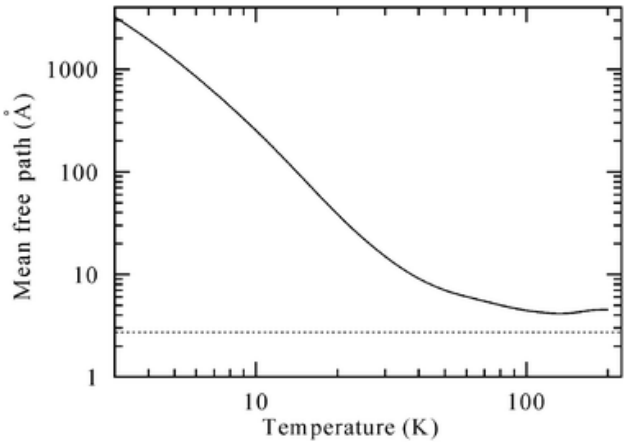

Figure 1.11: Mean free path vs temperature behaviour of phonons (Adapted from Krivchikov et al.[26])

A direct consequence of phonons' characteristics is that thermal conductivity is mainly limited by the material's thermal capacity in the very low

temperatures range while for high temperatures the mean free path plays the main role in limiting heat transport. This consideration is extremely important in the case of TE materials, one of the main strategies to improve their performances is in fact limiting the phonon mean free path by introducing large numbers of scattering sites.

1.3.3 Thermoelectric Effect

In order to simplify the very complex treatment of the thermoelectric effect a heuristic approach is followed. First of all, it is necessary to understand why temperature gradients can drive charge transport inside materials and this can be relatively easily comprehended referring to a simplified band structure model showing the material's carrier distribution around Fermi Energy.

If the two sides of a conductor under a temperature gradient are considered, it is easy to imagine that, following Fermi-Dirac Distribution, the hot side has a carrier population that is more spread out over energy with respect to the cold side. Computing the difference between the two, it becomes evident that an unbalance in carriers is present, this in turn generates a positive potential difference for energies higher than E_f and a negative one for energies below E_f. Now, if the density of states is exactly the same in the regions very close to Fermi Energy, then no net current flows: the same amount of electrons with energy higher than E_f would flow towards the cold side as the amount of electrons with Energy lower than E_f flowing towards the hot side. This situation is not very probable though, in almost all materials the density of states is not exactly specular with respect to the Fermi Energy and therefore a net current is produced. Depending on the shape of the DOS TE materials can be divided into two groups as n-type and p-type conductors. In the case of n-type the density of states is higher above the Fermy Energy and the net current is that of electrons flowing from the hot side towards the cold. On the other hand, p-type conductors have higher DOS at energies below E_f, their net current is then generated by electrons flowing from the cold side towards the hot one or, as it is more commonly visualised, holes flowing from the hot to the cold side.

This result is fundamental for the working principle of TE devices, in fact it becomes intuitive that only through the coupling of a p-type and an n-type material is it possible to close the circuit and extract energy from an applied temperature difference. The coefficient that best represents the thermoelectric effect is the Seebeck coefficient, defined as the potential difference generated between the two sides of a conductor for each unit

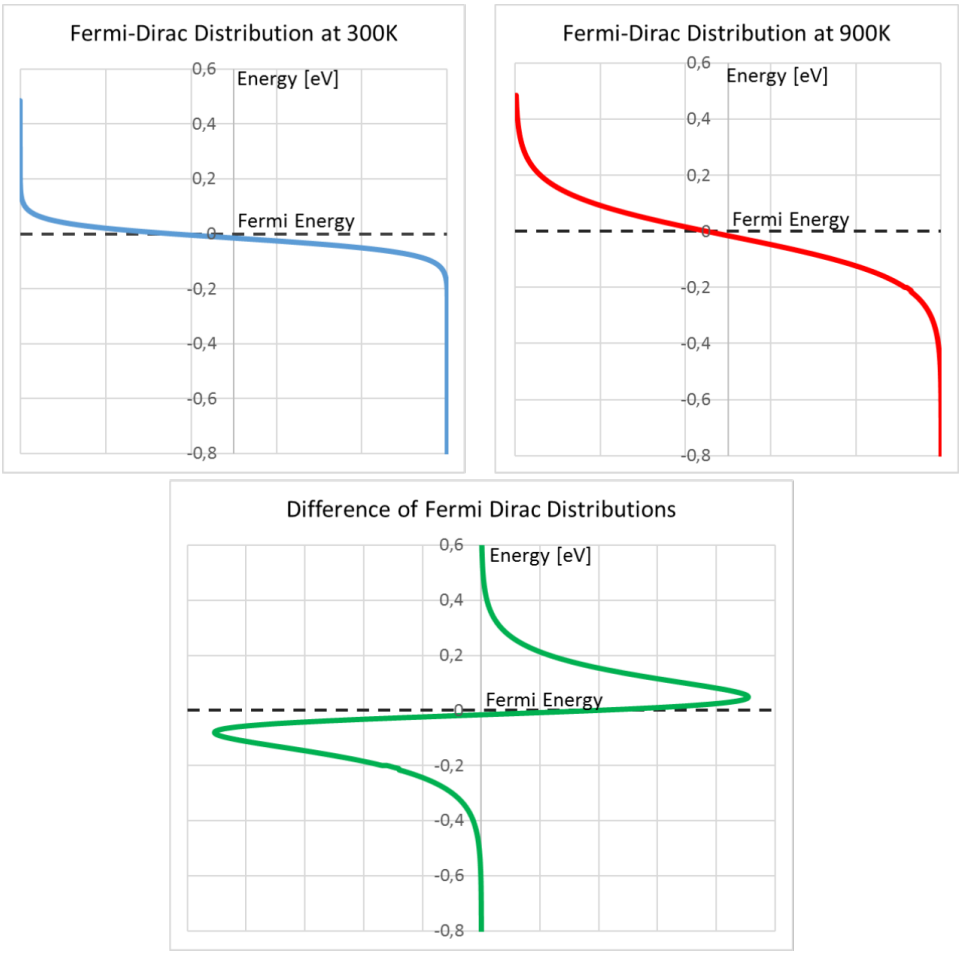

Figure 1.12: Fermi-Dirac Distributions at two temperatures and their difference above and below Fermi Energy

of temperature difference. A very simple current equation can be used to better understand the origins of this parameter and how it relates to other materials' properties.

$$I = \frac{1}{q} \cdot \int (f_1 - f_2) \cdot G(E) dE \tag{1.37}$$

Where q is the carrier charge, f_1 and f_2 are the Fermi-Dirac distributions of hot and cold side and G(E) is the conductance of an energy state. By solving the integral and expanding the two Fermi-Dirac distributions it is possible to define the current as coming from two contributions, one is the potential driven current already encountered in Section 1.3.1 and the other is directly

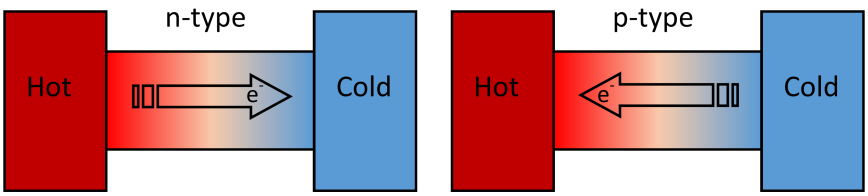

Figure 1.13: Comparison of electron flow in n-type and p-type semiconductor materials

related to the temperature difference between the points analysed.

$$I = G_V(\frac{V_1 - V_2}{q}) + G_S(T_1 - T_2) \tag{1.38}$$

Where G_V is the conductance due to potential difference and G_S is the conductance coming from temperature effects. They can furthermore be represented through the following expressions:

$$G_V = \int -\frac{df}{dE} \cdot G(E)dE \tag{1.39}$$

$$G_S = \frac{E - \mu}{qT} \cdot \int -\frac{df}{dE} \cdot G(E)dE \tag{1.40}$$

Where μ is the chemical potential of the material. It is straightforward to demonstrate in open circuit conditions, and referring to equation 1.38, that the Seebeck coefficient is simply a multiplier of a material's conductance that defines the portion of current driven by thermal gradient. It is therefore finally defined as:

$$S = \frac{G_S}{G_V} \tag{1.41}$$

Now that the Seebeck coefficient has been clarified it is possible to come to the most relevant quantity for this work, the Coefficient of Merit (zT). This quantity is actually dimensionless and can be easily defined through the predicted maximum output power of an ideal conductor subject to a temperature gradient. Imagining that the material acts as a voltage supplier, driven by the temperature difference, and considering its own internal resistance, then a simple equation can represent the maximum available power:

$$\Delta V^2 \cdot G_V = G_V \cdot \Delta T^2 \cdot S^2 \tag{1.42}$$

Still following this intuitive reasoning, it is possible to imagine that maintaining a temperature difference across a conductor requires energy, the

material will in fact transfer heat from the hot contact to the cold one. The ratio of maximum power output and power loss then becomes:

$$R = \frac{G_V \cdot \Delta T^2 \cdot S^2}{G_k \cdot \Delta T} \tag{1.43}$$

Where G_k is the Thermal Conductance of the material considered. So, by simply multiplying and dividing the obtained ratio by an average Temperature T, the final form of zT can be obtained:

$$R = \frac{G_V \cdot S^2 \cdot T}{G_{k\cdot}} \cdot \frac{\Delta T}{T} \tag{1.44}$$

$$zT = \frac{G_V \cdot S^2 \cdot T}{G_{k\cdot}} \tag{1.45}$$

Finally, it is possible to express this coefficient in the more common way, substituting the conductances with the material's conductivities.

$$zT = \frac{\sigma_V \cdot S^2 \cdot T}{k} = \frac{\sigma_V \cdot S^2 \cdot T}{k_L + k_e} \tag{1.46}$$

Where σ is the materials electrical conductivity and k is the thermal conductivity composed of lattice (k_L) and electronic (k_e) contributions, as already explained in Section 1.3.2. Analysing this coefficient, the main strategies for TE materials improvement become clear: it is necessary to increase the numerator as much as possible, thus either increasing Seebeck coefficient or the materials electrical conductivity are valid routes; the denominator should also be minimized, but being the denominator composed of two contributions k_L and k_e, improvement can only be obtained by reducing the lattice thermal conductivity. Decreasing the electronic contribution would have detrimental effects on the numerator as well since electrical conductivity and electronic contribution to thermal conductivity are strictly related.

1.3.4 zT Improvement Strategies

The TE performances are strongly influenced by the various transport characteristics of a material and, as already discussed in Section 1.3.3 the main factors are:

- Carrier Concentration and Distribution
- Carrier Mobility and Effective Mass
- Electronic Thermal Conductivity k_e

- Lattice Thermal Conductivity k_L

In order to maximize the zT coefficient these quantities need to be tailored and modified accordingly to their respective effects. This proves to be no easy task since many of these properties are conflicting. A very straightforward example is the effect of lattice thermal conductivity reduction: generally it has been shown that decoupling it from electrical conductivity is not simple and a decrease of the first has detrimental effects on the latter. Nonetheless, there are examples where the reduction of thermal conductivity far outweighs the repercussions on electrical conductivity, these systems are defined as phonon-glass electron-crystal (PGEC). In these particular structures the phonons perceive an high level of disorder, they undergo frequent scattering and their mean free path is reduced, on the other hand electrons are not affected by this long range disturbances and travel as if they were in a regular crystal. Often the approach to attain these results is the introduction of defects: these must be tailored so that their characteristic spacing is comparable to the phonons' mean free paths but larger than those of electrons, whose mean free paths are typically much shorter. A series of stratagems that allow the PGEC effect have been reported in literature over the years and the most important ones are discussed in the following sub-sections.

Disordered Unit Cells

There has been a large amount of studies devoted to the reduction of lattice thermal conductivity of TE materials by reducing the order of the crystal lattice. Various routes have been explored to achieve a high degree of disorder, with the introduction of interstitial sites, partial occupancies and voids being the most successful ones together with alloying of multiple materials. With respect to this last possibility a study by Wright showed, already in 1958, how substituting isoelectric anions and cations in Bismuth Telluride can lower thermal conductivity with no negative effects on the electrical conductivity. [50] Although this phenomenon has now been known for almost 60 years, it is still an active field of research and a number of studies are still being published suggesting novel composition and alloys to improve various base TE materials. [19] [9] [17] A peculiar case of disordered unit cells is constituted by the families of clathrates and skutterudites, these are materials containing large cage-like voids that can be filled with atoms called rattlers. The typical chlathrates composition is idealized as A_8E_{46}, where E are the host atoms and A the guest atoms, the former ones being usually from element groups 13 and 14 while the latter come from groups 1 and 2. Some

representative examples from literature are $Ba_8Ga_{16}Si_{30}$ [4] and $Sr_8Ga_{16}Ge_{30}$ achieving zT values over unity at 1100K [42] and, in both cases, it is possible to notice that the host atoms are actually two elements, leading to the more specific formula $A_8D_{16}E_{30}$. For skutterudites as well a general formula can be defined: M_4X_{12}, here the structure is much simpler but again intrinsic cages are formed arising from the octahedral cavities of the crystal. Usually the filling atoms in this class of materials are rare-earth, like in the case of $Nd_xCo_4Sb_{12}$ [28] or alkali metals like in $K_yCo_4Sb_{12}$. [37] Both for clathrates and skutterudites the guest atoms introduce anomalous vibration frequencies with respect to the rest of the lattice thus disturbing the phonon transmission and acting as scattering sites. Furthermore it is possible to have greater impact on thermal conductivity by producing only a partial filling of the voids, this allows a more random distribution of guest atoms in the crystal, resulting in high phonon scattering power thanks to additional defects and distortions. [41]

Complex Unit Cells

Another successful route for zT improvement is the construction of complex unit cells. It appears, though, that the key to the effect is not only the intrinsic complexity of the crystal but the various interactions and phenomena that arise as its consequence. For example, it has been demonstrated that a significant coefficient of merit improvement is possible for Bismuth Telluride by adding Caesium in its structure. [36] The resulting compound, $CsBi_4Te_6$, presents Cs layers that force the formation of Bi-Bi bonds that, in turn, both lower the material's band gap and modify the carriers effective mass bringing the maximum of zT to room temperature. Not only a change in temperature behaviour is obtained but the weakly bonded Caesium layers are considered to be a source of phonon scattering, thus lowering the lattice thermal conductivity of the material. Another example are the so called Zintl compounds, their complex structure is constituted by both covalent and ionic bonds and, while the first ones guarantee higher mobility of the carriers, the second ones allow the formation of complex structural units that slow down phonon propagation. Thanks to its great promise $Yb_{14}MnSb_{11}$ has already been accepted by NASA as future substitute of SiGe in satellite generators. [44] Finally compounds like Ag_9TlTe_5 and Tl_9BiTe_6 present a complex unit cell whose effect is also aided by the particular chemistry of Thallium, this element presents extremely soft bonds with its surrounding atoms resulting in very lossy vibrational energy transfer. [49] The materials obtained possess extremely low thermal conductivity, around 0.23W/mK

at room temperature, boosting their zT. The effect of these weak bonds is reflected in the crystals' mechanical properties as well, the materials are peculiarly soft with Young Moduli close to 23GPa, [27] much inferior to that of many common semiconductors.

Sub-Structured Materials

As already stated one of the main issues when acting on TE materials' properties is the risk of improving one and having as consequence the worsening of a second. In order to avoid this effect, materials with different regions, providing different functions, can be realised. This is not a new concept, being actually amply utilised in the field of oxide superconductors, and in the case of TEs it runs down to having a first component with very high mobility carriers, acting as the electron-crystal, and a second phase that becomes the phonon-glass counterpart. Many examples of this approach can be found in literature: Cobaltite Oxide presents Co-O metallic-like layers separated by insulating disordered layers, while the first sheets present very high mobility for an oxide based material, the insulating interposed ones still limit the overall thermal conductivity. [25] A compound that adopts a structure very similar to Cobaltite is $Ca_xYb_{1-x}Zn_2Sb_2$, this material is part of the Zintl family and is composed of sheets of covalently bound Zn-Sb interlaced with layers of disordered cations. Once again the more ordered covalent row will act as electron conductor while the disordered cation layer acts as phonon scattering site. [16] Unfortunately the zT coefficient obtained is not extremely high due to the relatively simple and regular crystal structure that has no long-range scattering effect.

Nano-Structuring

Theoretical and experimental evidences all lead to the belief that nanostructuring can greatly enhance the thermoelectric properties of materials. Already in the 1980s investigations were conducted on the reduced thermal conductivity of super-lattices with respect to their bulk counterparts, [54] but only in recent years more studies on the effect of boundaries have clarified the relationship between their concentration and the lattice thermal conductivity reduction. It is understood that the high density of interfaces behaves as a group of defects distributed all over the material, this results in a very short mean free path of phonons causing, in turn, a drop in thermal conductivity. A milestone for the nanostructuring of TEs is represented by Dresselhaus' work on bulk nanostructured SiGe, [13] demonstrating that it is possible to obtain a great decrease in lattice thermal conductivity even with disordered

grain boundaries and not only utilizing highly ordered superlattices. This paved the road for the exploration of a new class of materials: bulk nanostructured TEs, these are the category of choice for this work and they not only show great promise from a performance point of view but can also significantly lower the cost and time of production with respect to thin films. Pioneering results are those of Poudel [38] et al. and Heremans et al., [22] whose studies show that, starting from bulk Bismuth Antimony Telluride and Lead Telluride, it is possible to already significantly improve the zT coefficients by reaching a grain size in the order of hundreds of nanometers, achieving a peak zT of 1.4 for BiSbTe and of 1.2 for PbTe. The nano-sized grains are in both cases obtained by a simple ball-milling process and the so produced powders are afterwards compacted to form macroscopic pellets maintaining nanosized features.

Still considering the nano-structuring approach an idea widely proposed in literature is the mixing of two or more materials to achieve higher performances, this can go under the name of nano-compositing. As in the case of more common applications, like structural ones, compositing can be exploited to tailor and improve the properties of a matrix by adding a filler of different nature. One of the typical approaches in the world of TEs is the adding of a semi-conductor with different band-gap into a TE matrix, this leads to the formation of potential barriers causing energy filtering effects. [35] If the compositing is successful the direct result is an increase of Seebeck coefficient which in turns leads to higher zT values. Examples in literature include cases where the same particle shape is used for the matrix and the filler, as reported by Zou et al. [58] and Liu et al., [30] but also more complex composition including nano-rods and platelets are documented. [29] [45] Finally, in some instances, also the already cited effect of improving mechanical properties has been explored in TEs, a good example of this is the study by Akao et al. who added SiC whisker to Zn_4Sb_3 to obtain toughening effects. [1] In this work nano-compositing effects are explored and detailed explanations on how the materials in exam are fabricated are given in later sections.

1.4 Synthesis of Thermoelectric Materials

The synthesis step is one of the most critical in the whole processing of TE materials, it will in fact need to be accurately tailored to obtain the final desired composition, microstructure morphology and phase distribution. A very wide variety of both chemical and physical methods exist but, due to the scope of this work, the focus of the next sub-sections is on those utilized

for bulk TE materials production. It is possible to divide the synthesis approaches in the two broad categories that are commonly employed in nanostructure production: Top Down and Bottom Up.

1.4.1 Top Down Synthesis Schemes

When talking about top down techniques the characteristic feature is starting from a bulk material, that can be obtained following different approaches, and reducing it in size up to the wanted final dimensionality either by material removal or simple grinding. For what regards thermoelectrics it is possible to distinguish two main routes: melt alloying and mechanical alloying. Melt alloying is based on traditional metallurgy techniques, bulk ingots of the wanted final compositions are obtained by melting together and casting the various constituents, after these operations they are ground to a powder usually by extensive ball milling processes. Conversely mechanical alloying unifies these two steps, the starting materials are micron sized pure elemental powders that are ground together in a ball milling apparatus at high temperature. This kind of process achieves at the same time the final wanted composition, through alloying, and the desired size distribution. [43]

1.4.2 Bottom Up Synthesis Schemes

Bottom up approaches start from the constituents and build up the wanted materials to the desired final dimensionality and composition. The two main families in the case of TE materials are: deposition techniques and chemical reactions. Deposition techniques are mainly used to obtain thin film structures and are therefore not directly related to this work. Chemical routes, instead, are widely utilized to obtain bulk nanostructured TE materials and different research groups have used wildly diverse approaches with varying degrees of success. [34] The techniques that appear to yield best results regarding morphology, compositional control and particle size distribution are solution co-precipitation and solvo-thermal reactions. Not only do they guarantee a high degree of control through careful parameter tuning but they also lower the price of precursors with respect to the previously described top down approaches. It must be noticed, though, that every TE material composition requires different precursors and the same reaction is rarely adaptable to different materials classes, this significantly reduces the flexibility of the approach with respect to melting and mechanical alloying. On the other hand the chemical route is compatible with more environmentally friendly approaches and in recent years a trend going under the name of "Green Chemistry" has gained importance. While melting and alloying are

usually energy intensive, requiring heavy machinery and prolonged heating steps, these novel reactions are based on fast and energy efficient systems. The most important ones, in recent literature, are ultrasound assisted and microwave assisted reactors: they both allow energy to be delivered directly to the reagents thus removing the need for long solution heating steps, that require large amounts of energy, and reducing residence times. In this work, microwave-assisted thermolysis is utilized, therefore more detailed explanations on its features are given in other sections. In the following one the theory behind common chemical synthesis routes is clarified, thus allowing, later on, to better understand how microwave reactors work and how they can have an impact on synthesis.

1.4.3 Fundamentals of Chemical Synthesis

As previously illustrated, bottom up processes can be performed both in solid state or by wet chemistry but, for the scope of this work, only the second option is considered. It is possible to distinguish between the following cases:

- Metallic Nanoparticles Synthesis
- Oxide Nanoparticles Synthesis
- Semiconductor Nanoparticles Synthesis

The first variety presents the most straightforward reaction scheme, a chemical precursor containing one or more metallic atoms in oxidized form is reduced by a strong reducing agent:

$$[Me][Ox] + [Red] \rightarrow Me + [Red][Ox] \tag{1.47}$$

This is a very common route for the production of metallic nanodots, the stronger the reducing agent and the smaller the particles obtained. These kind of nanoparticles usually see the necessity of other agents in the reactions, most important of which are capping agents that will both protect the metal from re-oxidation and limit growth of the particles.

In the case of oxides the precursors are most commonly metal-alkoxides that follow a two step reaction kinetic, first they undergo a hydrolysis giving as products partially reacted metal-alkoxides having hydroxide substituent groups and alcohols.

$$[Me][Alkoxide]_m + H_2O \longrightarrow [Me][OH][Alkoxide]_{m-1} + Alcohol \tag{1.48}$$

Subsequently a condensation step takes place, two metal hydroxide react with each other generating an oxygen bond between the two metal atoms and expelling a water molecule:

$$[Me][OH]_n[Alkoxide]_{m-n} + [Me][OH]_l[Alkoxide]_{m-l} \longrightarrow [OH]_{n-1}[Alkoxide]_{m-n}[Me] - O - [Me][OH]_{l-1}[Alkoxide]_{m-l} + H_2O \tag{1.49}$$

These steps repeat themselves until an oxide particle is formed by progressive adding of metal-oxide bridges.

Thermolysis is the most common synthesis route for the production of semiconductor nanoparticles and quantum dots. It is based on the thermal decomposition of chemical precursors, that are otherwise stable at room temperature. The consequent freeing of atomic or ionic species and their reaction allows the nucleation of particles. Usually these processes are performed in anhydrous organic solvents, having very high boiling point, and reaching temperatures of 300-400°C. The typical reaction is between a metal in oxidized form (Metal Chlorides, Metal Oxides etc.) or metal-organic compound and a counterpart constituted either of a phosphine-semiconductor species, typically Trioctylphosphine (TOP) and a chalcogenide or a phosphine itself that releases its Phosphorus atom. The high temperatures mentioned act as driving force for the dissociation of the two precursors and kinetically favour a rapid nucleation of particles. Usually the obtained powders are capped by a second organic agent or by an excess of TOP. An exemplary process can be schematized as:

$$[Me][Organic/Ox] + [SemiCond.][TOP] \xrightarrow{Heat} [Me][SemiCond.] + [Organic/Ox][TOP] \tag{1.50}$$

The reaction is typically performed by a hot injection method, this consist in rapid introduction of a diluted precursor solution in a large bath of solvent kept at the wanted reaction temperature. The injection step causes an extremely fast nucleation thus producing a very high number of sites, limiting particle growth.

A thorough explanation of nucleation and growth kinetics and thermodynamics for nanoparticles and quantum dots is reported in the subsequent section.

Nucleation and Growth

When producing nanoparticles or quantum dots using wet chemistry, the process can be described through homogeneous nucleation and the driving

force for it is the supersaturation (σ) of the solution. This is defined through the following formula:

$$\sigma = \frac{C - C_0}{C_0} = \frac{C}{C_0} - 1 \tag{1.51}$$

Where C_0 is the saturation concentration and C is the actual concentration in the solvent. It is possible to show how nucleation is favourable when the concentration exceeds saturation through a simple Gibbs Energy Expression per unit volume:

$$\Delta G_V = -\frac{k_B T}{\Omega} ln(\sigma + 1) \tag{1.52}$$

Where Ω is the atomic volume of the growing species. It is at this point evident that:

- C $< C_0 \rightarrow \Delta G_V > 0$
- C $= C_0 \rightarrow \Delta G_V = 0$
- C $> C_0 \rightarrow \Delta G_V < 0$

Therefore nucleation can start when the third condition is satisfied, it is furthermore possible to introduce a second contribution to the energy change in the system: increase of surface energy during growth of a particle ($\Delta\mu_S$). This is always a positive value during nucleation and growth and acts in the opposite direction with respect to the volume contribution ($\Delta\mu_V$).

$$\Delta\mu_{Tot} = \Delta\mu_V + \Delta\mu_S \tag{1.53}$$

$$\Delta\mu_V = \Delta G_V \cdot V \tag{1.54}$$

$$\Delta\mu_S = \gamma_S \cdot A \tag{1.55}$$

Where V is the particle volume, A is the particle surface area and γ_S is the surface energy per unit area. In the assumption of spherical particles the total energy variation during nucleation and growth becomes:

$$\Delta\mu_{Tot} = \frac{4}{3}\pi r^3 \cdot \Delta G_V + 4\pi r^2 \cdot \gamma \tag{1.56}$$

It is possible to show how the surface contribution dominates at small particle radius while the volume contribution starts taking over at larger sizes. The critical dimensions, for which the nucleated particles become stable and do not tend to re-dissolve, are defined as r^* and the corresponding critical Gibbs Free Energy is $\Delta\mu^*_{Tot}$.

$$r^* = -\frac{2\gamma}{\Delta G_V} \tag{1.57}$$

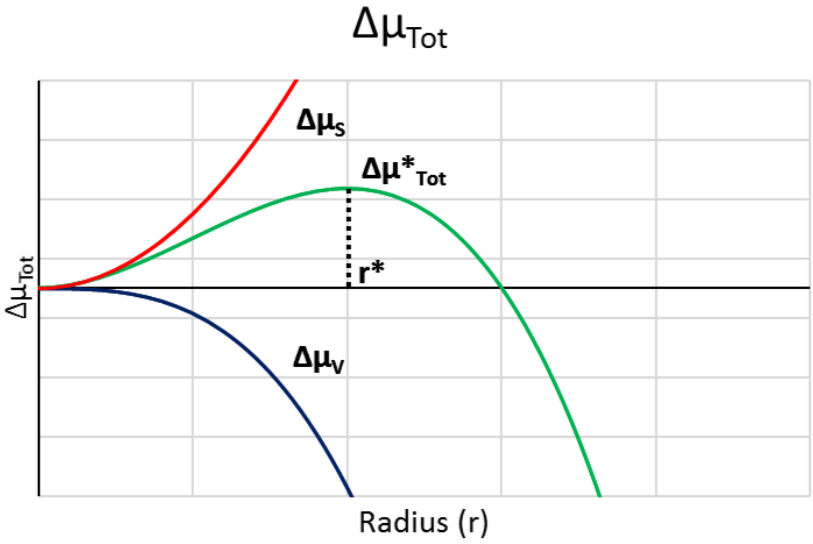

Figure 1.14: Nucleation and Growth Gibbs Free Energy Diagram

$$\Delta\mu^*_{Tot} = \frac{16}{3}\pi\frac{\gamma^3}{\Delta G_V^2} \tag{1.58}$$

The quantities previously defined are represented in a qualitative manner in Figure 1.14.

Finally it is possible to deal with some considerations on the kinetics. The process of nucleation described until now is followed by a growth period during which the nuclei that achieve stability can grow and form larger particles. It is evident that the larger the amount of species still in solution and the longer the formed particles can continue growing, not only, but in case of prolonged and slow chemical reactions the concentration can remain over the critical level defined as C* for a long period, thus allowing nucleation to take place. The outlined situation is not optimal, a large spread of particles dimensions is achieved and the control on them is relatively poor. The main reason behind procedures like hot injection and microwave assisted reactions lies exactly in the described phenomenon, the sharper and the more explosive the initial nucleation and the smaller and more homogeneous the nanoparticles obtained. It is possible to qualitatively schematize the concentration trend in a slow reaction followed by prolonged nucleation, Figure 1.15 blue line, and in a fast chemical reaction followed by burst nucleation, Figure 1.15 red line. In the second case the rapid depletion of growing species limits the nucleation time and the reaction can be rapidly stopped to freeze the particles dimension. Both capping and quenching are valid

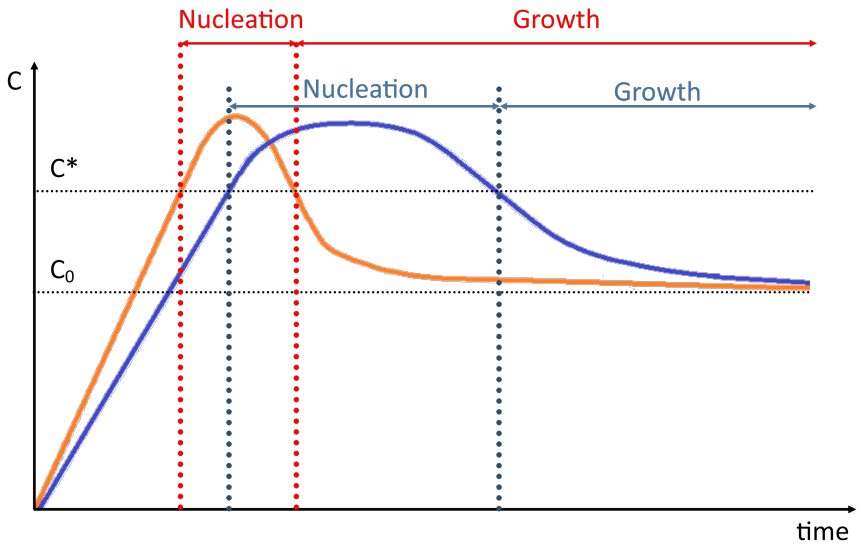

Figure 1.15: Nucleation and Growth phases depending on concentration

alternatives to stop ripening or further growth and they can be performed without significantly reducing yield. The great majority of the species is, in fact, already incorporated in the particles when the synthesis is stopped.

1.5 Objectives

TE materials have been subject of research for almost 200 years, but only recent advancements in nanotechnology have allowed the application of concepts previously formulated. The figure of merit (zT) can be significantly improved with respect to the bulk limit by artificially reducing the lattice thermal conductivity of a material (k_L). This effect is achievable through different means but what is going to be explored in this work is mainly nano-sizing of the crystalline structure. In particular nano-grained materials present increased phonon scattering due to high grain boundary density, leading to a significant improvement of zT. In this work we aim at obtaining a simple, reliable and up-scalable production route for nano-structured Copper Selenides. The selected method is a microwave (MW) assisted thermolysis, as mentioned in previous sections, that furthermore can improve energy efficiency with respect to other techniques. Various routes to further improve the figure of merit are to be explored, mainly focusing on nano-compositing approaches and trying to understand the impact that different phases can have on the TE performance. The optimization of a flexible fabrication route for the composites is also pursued, aiming at obtaining

a process that can be easily tuned for various compositions and matrix to filler ratios. The final goal is obtaining a category of TE materials that can deliver a high zT due to controlled and precise nano-structuring and nano-compositing, while at the same time employing a low cost, energy efficient and high throughput production method. This can, in time, lead to everyday applications that have been precluded up until now due to the unsustainable production costs.

Chapter 2

Experimental

2.1 TE Material Synthesis

The powders are obtained following a thermochemical process based on wet chemistry and assisted by microwave irradiation. In the following sections the apparatus is described.

2.1.1 Microwave Reactor

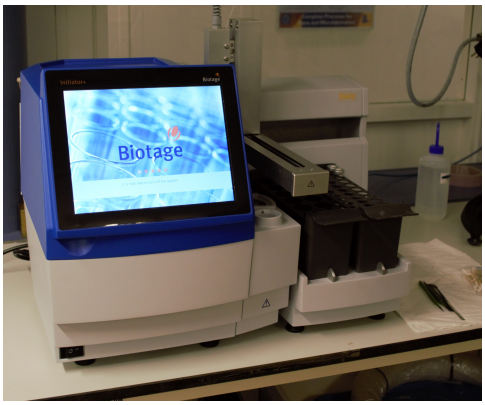

Figure 2.1: Microwave Reactor Initatior+ by Biotage®

The reactor utilized is an Initatior+ produced by Biotage®, the machine is composed of a reaction chamber, a control panel and a robotic arm for sample handling. The reagents are loaded into a quartz reaction vial with a maximum capacity of 20ml, the vial is then sealed with a silicone septum and inserted into the machine's holding racks. From this point onwards the process is completely automated, the vial is handled by the robotic arm and inserted in the reaction chamber, where stirring can be performed. The

irradiation with the selected microwave power is performed at operational temperatures ranging from 50°C up to 250°C. The internal pressure in the vial is limited to 30 bars. The machine allows both a temperature history control and a pressure control, depending on the wanted reaction parameters.

2.1.2 Vacuum Drying Oven

Figure 2.2: Vacucell 55 Vacuum Drying Oven

The Vacucell 55 vacuum drying oven is employed for sample drying after the washing steps. The apparatus consists of a refractory chamber heated by a resistive element. The pressure inside the chamber can be lowered to less than 10% of atmospheric, while a thermal history can also be applied and tailored to the specific needs of each material.

2.1.3 Synthesis Operating Procedures

In the following subsections the operating procedures for the production of $Cu_{1.8}Se$ and Cu_2Se are described. Explanations on how the two routes have been optimized can be found in Section 3.1.

Pure $Cu_{1.8}Se$

All the chemicals used are purchased and employed as received: Copper Acetate Monohydrate; Selenium powder (99.5% 100mesh); Trioctylphosphine (97%); Oleic Acid (90%); 1-Octadecene (90%). In addition to these chemicals one 20ml quartz vial from Biotage® and its respective silicon septum are

needed. Initially 9.70 mmol Copper Acetate and 4.85 mmol Selenium powders are added into a 20ml quartz microwave vial, then 4ml 1-Octadecene and 8ml Oleic Acid are poured in as organic dispersing solution, finally a magnetic stirrer bar is inserted. The vial at this point is sealed with a silicone septum and, to reduce oxygen contact, 2.5ml Trioctylphosphine are injected in the mixture perforating the septum by a syringe. The obtained dispersion is kept under stirring at 600rpm for 2 minutes and finally inserted in the microwave reactor. Keeping in mind that each vial yields around 1g of final product, the process can be repeated as many times as needed, preparing therefore the number of vials corresponding to the wanted amount of powders. The instrument keeps each vial under further stirring for 5 minutes before beginning microwave irradiation, this rapidly brings the temperature to the set value of 200°C, temperature maintained constant for 5 minutes of reaction time. Curves representing the microwave parameters are reported in Figure 2.3.

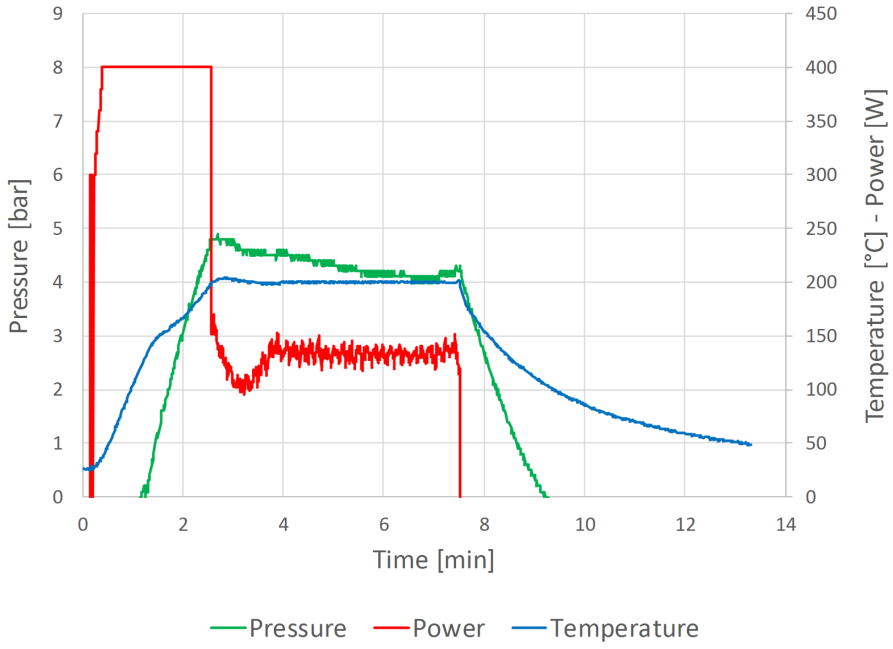

Figure 2.3: Representative Microwave plot reporting the curves of Power, Temperature and Pressure for the synthesis of $Cu_{1.8}Se$

The vial is then automatically cooled by compressed air and extracted from the reaction chamber by the machine's robotic arm. At this point the reactor will proceed in the same manner for all the vials present in the holding rack. After the heating process the dispersion colour changes

from dark green-bluish to a dark black-brownish tint with black-brownish powder precipitates. The obtained powders are then washed several times using a 3:1 mixture of Methanol and Hexane and recollecting the powders by centrifuging between washing steps. The number of rinsing steps is kept between 3 and 5 depending on the amount of powders added to the rinsing vessel. Checking of the colour of the waste rinsing solution helps in ensuring total removal of the by-products. Finally the powders are placed in the vacuum drying oven at a temperature of 60°C and a pressure lower than 10% of atmospheric for 12 hours to ensure total solvent evaporation. The particles are at this point ready for sintering.

Pure Cu_2Se

All the chemicals used are purchased and employed as received: Copper Acetate Monohydrate; Selenium powder (99.5% 100mesh); Trioctylphosphine (97%); Oleic Acid (90%); 1-Octadecene (90%). In addition to these chemical one 20ml quartz vial from Biotage® is needed for each 1g of final product and 1 other vial to be utilised for the preparation of TOP-Se stock solution, their respective silicon septa are also needed. Initially 9.70 mmol Copper Acetate are added into a 20ml quartz microwave vial, then 4ml 1-Octadecene and 8ml Oleic Acid are poured in as organic dispersing solution and a magnetic stirrer bar is inserted. The vial at this point is sealed with a silicone septum and kept under stirring for a minimum of 120 minutes at 600 rpm. Meanwhile, the amount of Selenium powder needed for the wanted number of vials is added to a 20ml quartz vial, following the proportion of 4.85 mmol for each vial of final product. Said vessel is then sealed with a silicon septa and 0.5ml of TOP are injected with a syringe for each mmol of Se powder. Selenium dissolves immediately and 2.5ml of the solution can be injected in each of the sealed Copper Acetate mixture microwave vials by a syringe. The obtained mixture is kept under stirring at 600 rpm for 2 minutes and finally inserted in the microwave reactor. The instrument keeps each vial under further stirring for 5 minutes before beginning microwave irradiation, this rapidly brings the temperature to the set value of 250°C, temperature maintained constant for 5 minutes of reaction time. Curves representing the microwave parameters are reported in Figure 2.4. The vial is then automatically cooled by compressed air and extracted from the reaction chamber by the machine's robotic arm. At this point the reactor will proceed in the same manner for all the vials present in the holding rack. After the heating process the dispersion colour changes from dark green-bluish to a dark black-brownish tint with black-brownish powder precipitates. The obtained

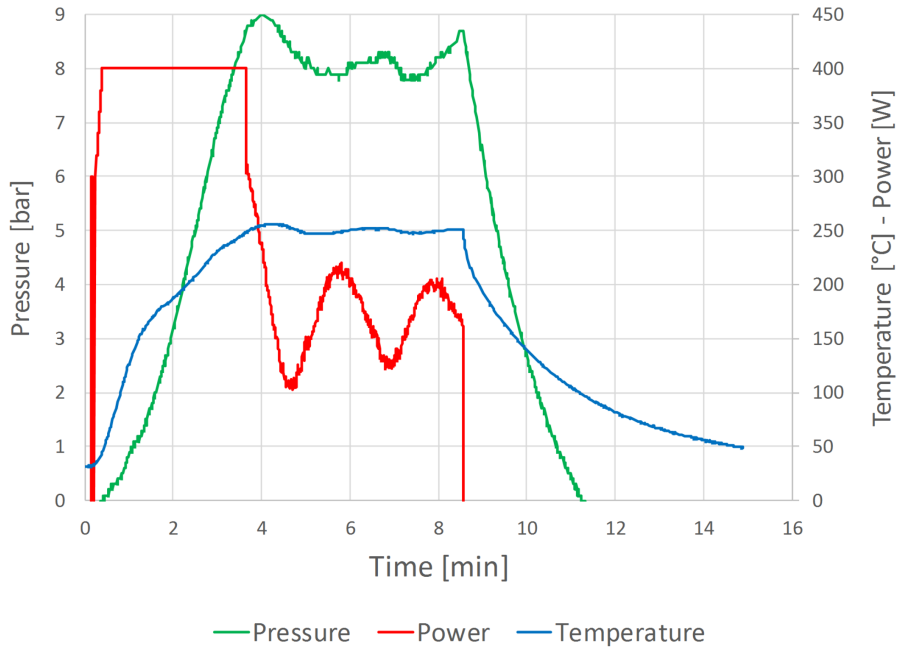

Figure 2.4: Representative Microwave plot reporting the curves of Power, Temperature and Pressure for the synthesis of Cu_2Se

powders are then washed several times using a 3:1 mixture of Methanol and Hexane and recollecting the powders by centrifuging between washing steps. The number of rinsing steps is 3 to 5 depending on the amount of powders added to the rinsing vessel. Checking of the colour of the waste rinsing solution helps in ensuring total removal of the by-products. Finally the powders are placed in the vacuum drying oven at a temperature of 60°C and a pressure lower than 10% of atmospheric for 12 hours to ensure total solvent evaporation. The particles are at this point ready for sintering.

2.2 Consolidation of TE Nanopowder

The obtained powders need to be compacted in a pellet form for thermoelectric properties measuring, the technique selected for this step is spark plasma sintering and the reasons behind this choice are clarified in the next section.

2.2.1 Spark Plasma Sintering

The SPS apparatus consists of a chamber containing a hydraulic press with steel plates and connected to a high current pulsed DC supply. The samples, in powder form, are loaded in a graphite die that is subsequently placed between the hydraulic press plates. The temperature and loading parameters can be controlled and the machine employed is able to sinter specimens from few hundreds to 2000°C while applying loads from 2 to 20kN.

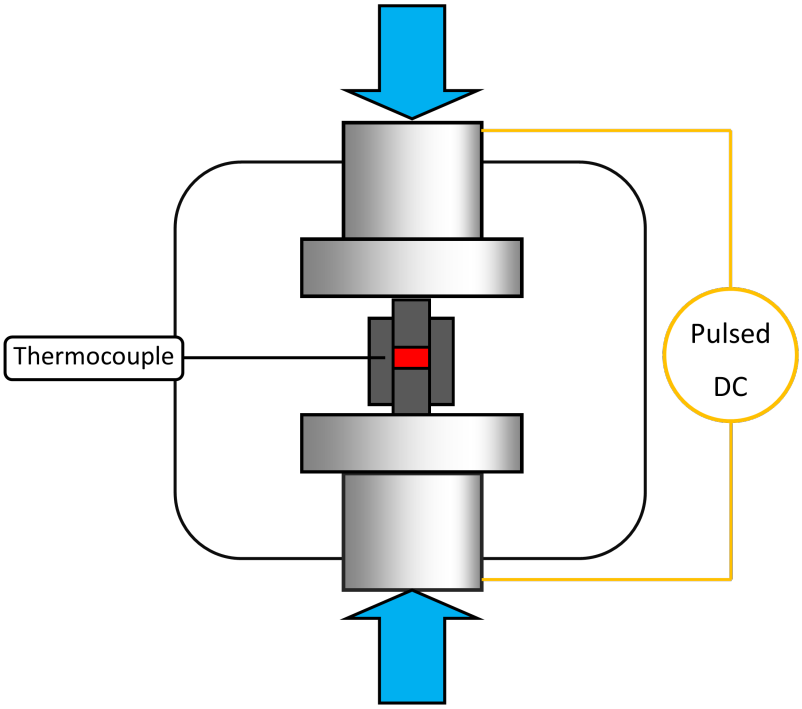

Figure 2.5: Scheme of the Spark Plasma Sintering apparatus

The size of the die utilized is selected according to the wanted final product and the composition and pressure of gases inside the chamber can also be chosen suitably. With this system it is possible to pass a large amount of current directly through a conductive sample, while also applying the wanted uniaxial pressure. The main advantage of this method over traditional sintering are reduced processing times and required pressures due to the direct heating of the powders caused by Joule effect. In traditional sintering the heat flows from the external furnace towards the centre of the dies, causing temperatures gradients and requiring therefore a holding time for temperature homogenization. In this case, instead, the heat is generated directly inside the powder specimen allowing a superior control and faster heating rates. While the temperature can be controlled in average over the

whole sample, it is also true that there will be local heating concentrated in the regions of higher resistance: initially the effect is due to plasma discharge where particles are in close vicinity, in later stages it is related to the relatively high resistance of the meniscus formed between them.

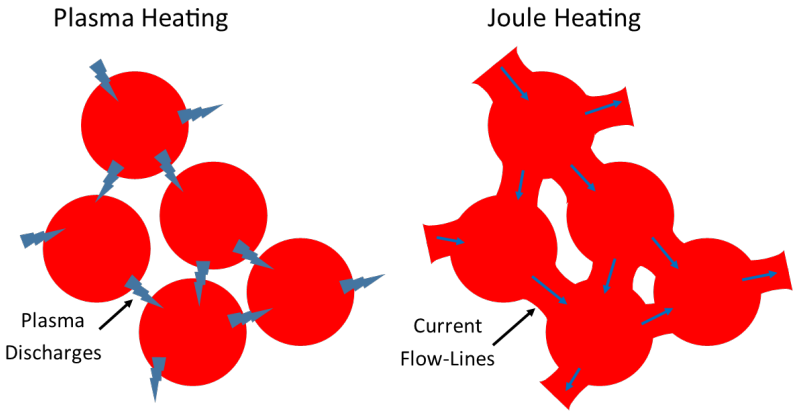

Figure 2.6: Local Heating in Spark Plasma Sintering

Local heating is a positive feature as these areas are, incidentally, those that require the most thorough sintering since they present higher porosity. It is evident, then, that the technique allows a better final compaction with reduced grain size growth and sample alteration, both fundamental requirements when a conservation of nano-features is desirable.

2.3 Characterization

2.3.1 X-Ray Diffraction

XRD is employed to identify the crystalline phases obtained both before and after compaction. The apparatus used is an Empyrean produced by PANalytical, it utilizes a Cu k-alpha source at 1.54Åwavelength and a Bragg-Brentano geometry is employed. The method allows a rapid analysis of specimens in powder form, identifying the phases thanks both to the position and intensity of the measured diffraction peaks. This technique is based on the assumption of completely isotropic samples, which is surely respected in powder form and, even in the case of sintered samples, can still be considered valid since a very high degree of multy-crystallinity is mantained guaranteeing fairly high isotropicity.

Figure 2.7: Empyrean X-Ray Diffraction Apparatus by PANalytical

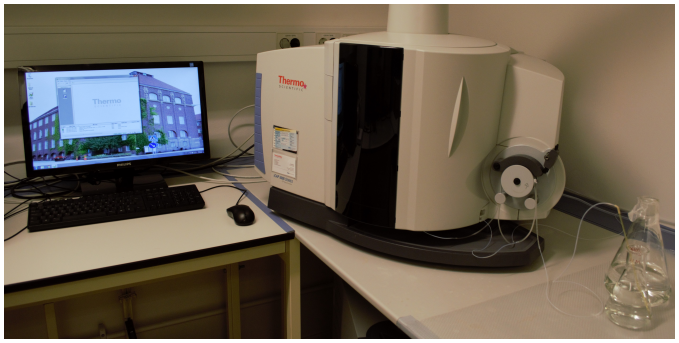

Figure 2.8: iCap6500 Inductively Coupled Plasma Emission Spectrometrometer by ThermoScientific

2.3.2 Inductively Coupled Plasma Emission Spectrometry

The instrument employed is an iCap 6500 produced by ThermoScientific, and allows detection of elements dissolved in aqueous or organic solvents up to concentrations lower than 1ppb. The principle the machine is based on is the measuring of atomic or ionic emission spectra of a very diluted solution containing metallic or semiconducting species. Said solution is sprayed through a plasma that immediately causes the dissociation of any bond present and excites the atoms or ions obtained, causing emissions at characteristic wavelengths. A series of monochromators sweep through a range of wavelengths while a CCD detector counts the number of photons emitted at each radiation frequency. The equipment composes in this manner the

emission spectrum of the sample and allows measuring of the concentrations of the species present. In this study the instrument is utilized to verify the respective concentration of Copper and Selenium in the prepared samples. While XRD allows the detection of crystalline phases, it is impossible to be sure of the precise stoichiometry, for two main reasons:

- Copper Selenides have high tolerance to element deficiency and will therefore maintain a specific crystalline structure even when stoichiometry is not respected.
- XRD is not able to detect amorphous phases that might be present in the sample and even extremely small crystallites might be under the detection limit.

In order to by-pass these limitations ICPES is used: the samples are dissolved in concentrated Nitric Acid and then diluted in deionized water up to concentrations in order of few ppm. The obtained solutions are tested against a reference, thus revealing the average relative concentration of the two elements, Copper and Selenium.

2.3.3 Scanning Electron Microscopy

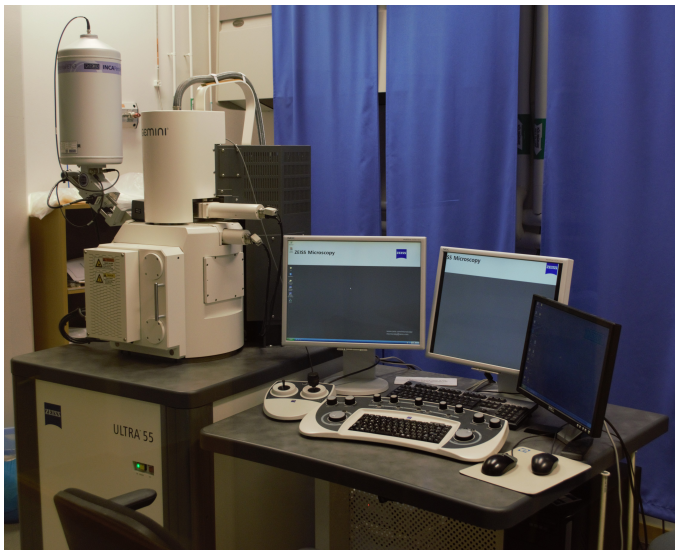

Figure 2.9: ULTRA55 Scanning Electron Microscope System by Zeiss and Oxord X-MAX Energy-dispersive X-Ray Spectrometer

SEM is employed to analyse the morphology and particle size of the dried powders and the fracture surface of samples after compaction; both

specimen types are prepared on carbon tape to avoid charging effects. The microscope is an ULTRA55 produced by Zeiss and is based on a thermal field emission source. The instrument allows reading of both secondary electrons and back-scattered electrons signals. An Oxord X-Max Energy-dispersive X-Ray spectroscopy apparatus is also integrated into the system and is employed for a semi-quantitative measurement of the local sample composition.

2.3.4 Differential Scanning Calorimetry

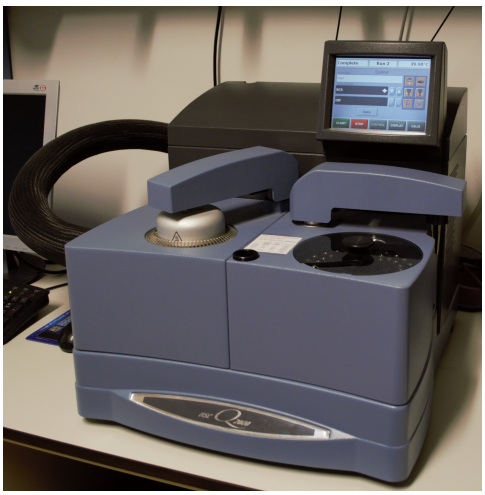

Figure 2.10: DSC2920 Differential Scanning Calorimeter by TA Instruments

The instrument employed is a DSC2920 produced by TA Instruments, it allows measurements from room temperature up to 725°C. As it is known DSC allows the precise individuation of all exothermic and endothermic phenomena taking place in a material during heating and cooling. In this case DSC is used to measure the phase transition points of the produced materials: Copper Selenides present a complex phase diagram and phase transitions may take place at different temperature depending on composition. Exploratory measurements are thus needed in order to tailor the subsequent steps, for example sintering parameters, to the specific material.

2.3.5 Thermogravimetric Analysis

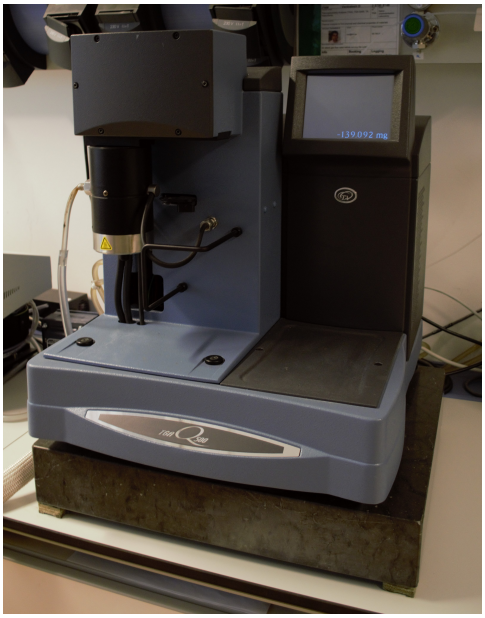

Figure 2.11: TGA Q500 Thermogravimetric Analysis Apparatus by TA Instruments

This technique proves necessary to verify the thermal stability of the materials. TGA allows, in fact, the measuring of mass loss or gain under different atmospheres when the samples are heated up. Both kinds of mass variation are attributed to some sort of sample degradation, be it physical evaporation or chemical reactions taking place between it and the atmosphere in the chamber. The instrument employed is a TGA Q500 produced by TA Instruments and allows measurement in various atmospheres from room temperature up to 1000°C.

2.3.6 Transport Properties Measurements

The measurement of the Electrical Transport properties is performed at the Technical University of Denmark (DTU): the sample is cut in the shape of a bar (usually 4x4x9 mm^3) and placed in a ZEM-03 Apparatus from ULVAC Technologies. The instrument consist of two heating plates and two electrodes in direct contact with the sample, everything is enclosed in an Infrared Furnace that performs a temperature scan while the heating plates mantain a temperature gradient along the bar length. The apparatus extracts both Seebeck coefficient and electrical conductivity curves from 250K to 900K at the same time.

Chapter 3

Results and Discussion

3.1 Synthesis and Optimization

Copper Acetate Monohydrate, Selenium Powder (>99.5%), 1-Octadecene (90%), Oleic Acid (90%) and Trioctylphosphine (97%) are utilised. All chemicals are purchased from Sigma Aldrich and used as received. Several optimization steps are performed to achieve the wanted composition and phase distribution. In the following sections the general process and the optimization stages are described, the reasons behind certain changes in the procedures are also discussed.

3.1.1 Microwave Assisted Thermolysis Mechanism

Microwave assisted thermolysis can be considered a variation of the last process described in Section 1.4.3. In this segment the specific reaction employed in this work is described to better understand the following optimizations. It is possible to divide the reaction in two steps:

1. Precursors formation
2. Reaction of the precursors

The first step is further composed of two reactions that can happen side by side or be performed in different vessels:

1. Precursors formation
   (a) Metal-organic formation
   (b) Bonding of a VI Group element (Chalcogens) with a ligand

(a) Initially a metallic salt is present, in this specific case Copper Acetate, the species is exposed to an Organic compound, Oleic Acid, and reacts forming a metal-organic, Copper Oleate. The reaction described gives Acetic Acid as by-product.

$$Cu(CH_3COO)_2 + 2Oleic\ Acid \rightarrow Cu(Oleate)_2 + 2CH_3COOH \quad (3.1)$$

(b) An element of the Chalcogens group, in this specific case Selenium, bonds with a ligand, Trioctylphosphine. The ligand is chosen to be compatible with the metal counterpart, therefore, in case of metal-organic, an organic species is selected. The Selenium powder dissolution in TOP is typically rather vigorous and gives as result Trioctylphosphine Selenide.

$$Se^{(Me)} + TOP \rightarrow Se(TOP) \quad (3.2)$$

The second step of the reaction can now take place between the obtained precursors. High temperatures are needed to allow the dissociation of the metal-organic species and its subsequent reaction with the chalcolgen. The reaction yields a semiconducting material in form of nano-powders, Copper Selenide, and two by-products, Trioctylphosphine Oxide and Oleic Anhydride. [6]

$$xCu(Oleate)_2 + Se(TOP) \xrightarrow{Heat} Cu_xSe + (TOPO) + OleicAnhydride \quad (3.3)$$

In presence of water the Oleic Anhydride can further react to yield Oleic Acid once again. In order to achieve a rapid nucleation, the necessity of which was described in Section 1.4.3, a hot injection method is usually employed, this has the great advantage of limiting growth time by causing a burst nucleation but reproducibility is mainly determined by human factors. On the other hand, in microwave assisted thermolysis the energy needed for the metal-organic dissociation is provided by microwave irradiation, the heat delivered and temperatures achieved during reaction are closely controlled by the machine and are, therefore, much less subject to variation, thus increasing reproducibility. Furthermore, hot injection employs a large hot bath of solvent even to produce relatively low amounts of product, resulting in a time and energy intensive process. Microwave irradiation, instead, rapidly brings the whole reaction solution up to the desired temperature in a single vessel. Finally, the particles form by burst nucleation once the critical temperature is achieved, corresponding to the metal-organic dissociation by thermal energy. This guarantees the production of small particles by strongly limiting the growth period. In the following sections the exact steps that lead to process optimization are described.

3.1.2 Optimization of Phase Purity

As already mentioned an optimization proves necessary to obtain the two standard procedures reported in Section 2.1.3. Here the first method followed is reported: 9.70 mmol Copper Acetate and 4.85 mmol Selenium powders are added into a 20ml quartz microwave vial, then 4ml 1-Octadecene and 8ml Oleic Acid are poured in as organic dispersing solution. The vial at this point is sealed with a silicone septum and 2.5ml Trioctylphosphine are added to the mixture by syringe injection to reduce oxygen contact. The obtained dispersion is kept under stirring at 600rpm for 2 minutes and finally inserted in the microwave reactor. This process can be repeated as many times as needed to obtain the wanted amount of powders, keeping in mind that each 20ml vial yields around 1g of final product. The instrument is set for 5 minutes of pre-stirring before beginning microwave irradiation, this rapidly brings the temperature to the set value of 250°C, temperature maintained constant for 5 minutes of reaction time, curves representing the microwave parameters are reported in Figure 3.1. The vial is then automat-

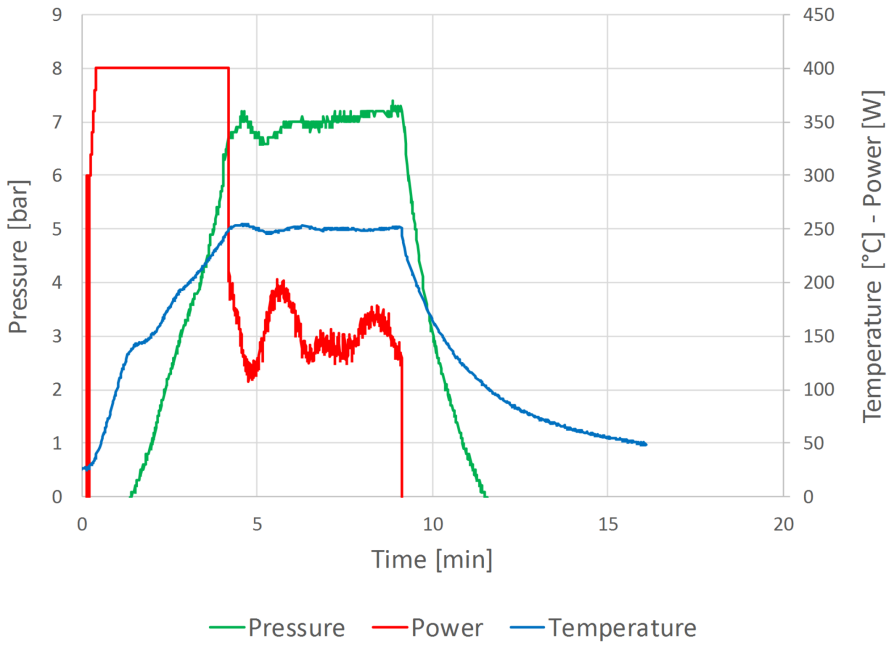

Figure 3.1: Representative Microwave plot reporting the curves of Power, Temperature and Pressure for the synthesis of Cu_2Se + x% $Cu_{1.8}Se$

ically cooled by compressed air and extracted from the reaction chamber by the machine's robotic arm. At this point the microwave proceeds in the

same manner for all the vials present in the holding rack. As soon as the vial is extracted from the microwave a change in the mixture's colour is evident and confirms that a reaction takes place, the blue-green dispersion changes to a very dark brown-black colour with a thick layer of black-brownish powder precipitates at the bottom of the vial. The obtained powders are rinsed several times following the procedure described in Section 2.1.3 and finally dried. The first test performed is the XRD analysis, the obtained 2θ patterns are compared with literature to individuate the phases present, as can be seen from the graph in Figure 3.2, the results highlight the presence of two crystallographic phases: Cu_2Se and $Cu_{1.8}Se$. This is an unwanted result

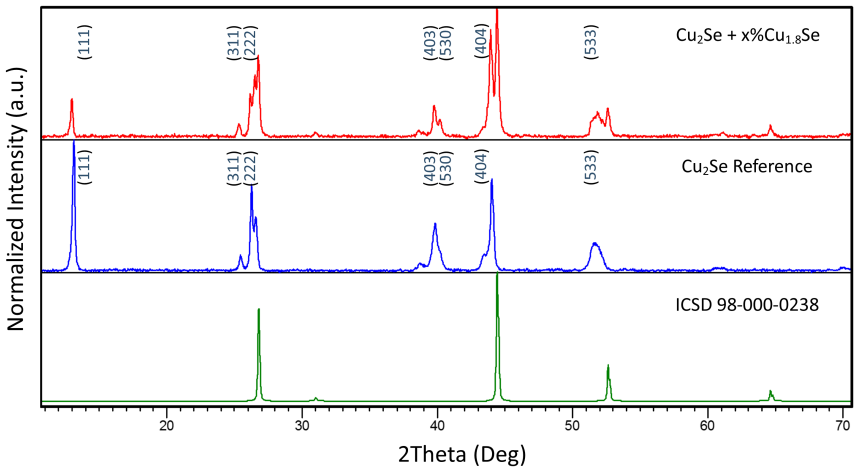

Figure 3.2: XRD patterns of produced powders compared to pure Cu_2Se phase from literature [18] and ICSD Standard Reference Pattern of $Cu_{1.8}Se$ (ICSD 98-000-0238)

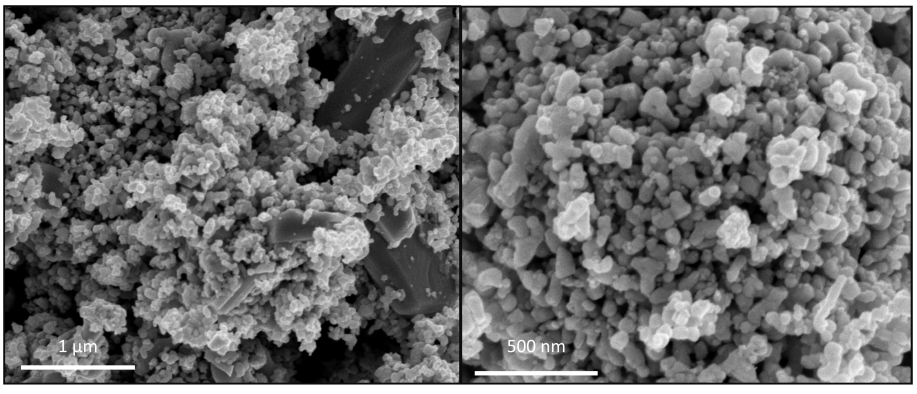

Figure 3.3: SEM micrographs of the Cu_2Se + x% $Cu_{1.8}Se$ sample at different magnifications

since it allows a relatively poor control on the sample composition. Studies employing SEM are also performed to check the dimensions of the particles and their morphology. The average size is around 60nm but a relatively wide distribution is present, with some particles as small as 5-10 nm and a few as big as 1μm. The shapes are quite irregular with no distinguishable geometrical feature that could be reconducted to the crystal structure of the material. The random shape is attributed to the extremely short time of reaction that does not allow significant growth and atomic rearrangement, the species, therefore, do not have the time to build a well defined shape dominated by crystal geometry. On the other hand a very high degree of crystallinity is detected by XRD suggesting that the random shapes are conglomerates of smaller crystallites. In conclusion although dimension and morphology are satisfactory the mixture of phases obtained is not adequate to the needs of this study, it is thus necessary to modify reaction in order to obtain a single phase.
The reasons behind the mixture of phases obtained are investigated, the main culprit is believed to be the low availability of Copper Oleate during the reaction step. Probably a strongly Copper deficient $Cu_{2-x}Se$ phase is initially formed due to its higher stability at the reaction temperatures, the crystallographic phase obtained will be so strained, though, that a conversion to the $Cu_{1.8}Se$ phase takes place. This step releases the internal stress and the phase separation continues until equilibrium is reached between the now Cu enriched $Cu_{2-x}Se$ and the newly formed $Cu_{1.8}Se$. The reason behind the low Copper Oleate availability is in turn believed to be caused by incomplete Copper Acetate dissolution in the Oleic Acid and 1-Octadecene mixture. These conclusions give rise to two approaches:

- Change in Reaction Temperature and Time
- Pre-dispersion of Copper Acetate in Oleic Acid and 1-Octadecene

3.1.3 Synthesis and Characterization of $Cu_{1.8}Se$

In order to explore its effects on the availability of Copper during the reaction, the temperature is lowered expecting a lower concentration of Cu_2Se phase with respect to $Cu_{1.8}Se$. This proves to be the case and it is even demonstrated by XRD analysis that pure $Cu_{1.8}Se$ can be obtained following the procedure reported in Section 2.1.3. The only difference with respect to the phase mixture is thus related to the reaction temperature that is lowered to 200°C. It is believed that, at this temperature, only a partial conversion of Copper Acetate to Copper Oleate is possible thus Copper availability re-

mains low and only the $Cu_{1.8}Se$ phase can be produced. As already stated the obtained powders are analysed by XRD and a comparison with reference diffraction pattern, reported in Figure 3.4, shows the high purity single phase obtained.

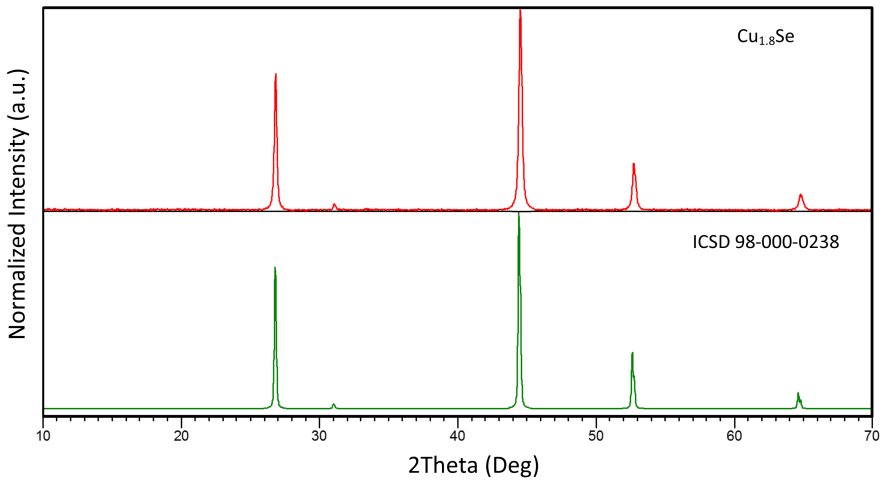

Figure 3.4: XRD patterns of $Cu_{1.8}Se$ powders as produced compared to ICSD Standard Reference Pattern of $Cu_{1.8}Se$ (ICSD 98-000-0238)

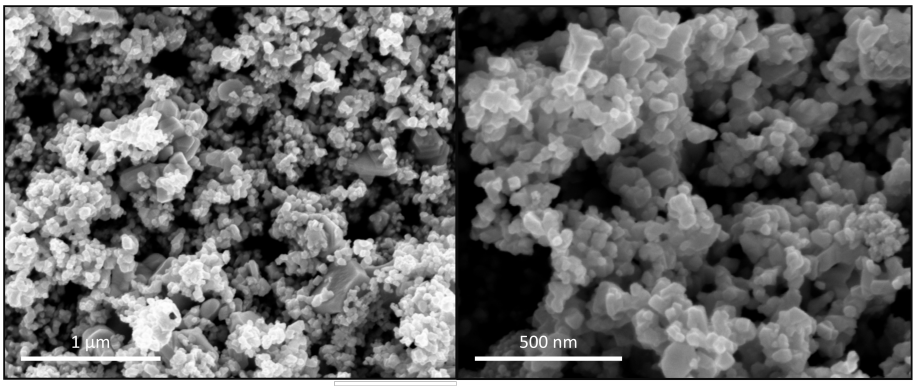

Figure 3.5: SEM micrographs of $Cu_{1.8}Se$ sample at different magnifications

The sample also undergoes DSC analysis: after a first cycle, during which the grains rearrange and a very noisy signal is gathered, the subsequent ones perfectly overlap and no phase transitions are visible. This is as expected from theory since only Cu_2Se is a phase-change material. The mentioned thermograms are not reported since they do not add much to the discussion, consisting only of a perfect heating-cooling loop from 25°C to 300°C. Once again also Electron Microscopy is performed and both morphology and aver-

age size of the particles are studied. The size distribution shows an average of around 60 nm with the presence of some smaller particles, 5-10nm and a few larger ones as well, reaching micrometer size. In this case ICPES is performed in addition to check the final powder composition, the results show that even maintaining the $Cu_{1.8}Se$ crystallographic phase, the material is copper deficient and can be more accurately described as $Cu_{1.8-x}Se$. The results obtained reinforced the conviction that the parameter that dominates phase selection is the copper availability and opened the road for the production of a single phase Cu_2Se described in following section.

3.1.4 Synthesis and Characterization of Cu_2Se

Initially longer reaction time were experimented with hoping in the progressive release of Copper from the reagents which would allow the reconversion of $Cu_{1.8}Se$ to Cu_2Se. Unfortunately XRD performed on samples with holding time of 5, 10 and 15 minutes show only minor differences in phase distribution. The increase of reaction temperature is also considered as valid alternative but is not possible due to the equipment limitations, thus a new option arises. A prolonged mixing step of Copper Acetate in Oleic Acid and 1-Octadecene mixture is believed to allow thorough dispersion of the precursor, thus facilitating conversion to Copper Oleate during the heating step. This reasoning proved successful as demonstrated by the XRD graph reported in Figure 3.6, comparing the reference diffraction pattern of Cu_2Se [18] and the powders produced. The sample also undergoes

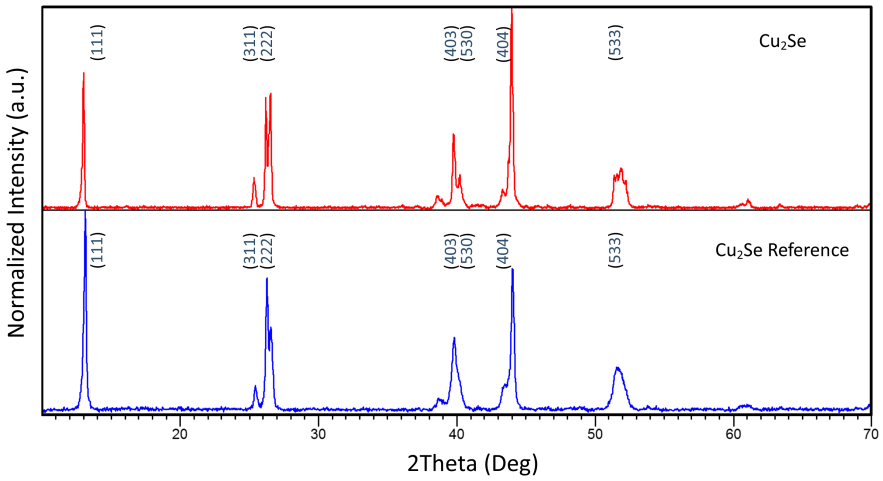

Figure 3.6: XRD patterns of produced powders compared to Reference Pattern from literature [18]

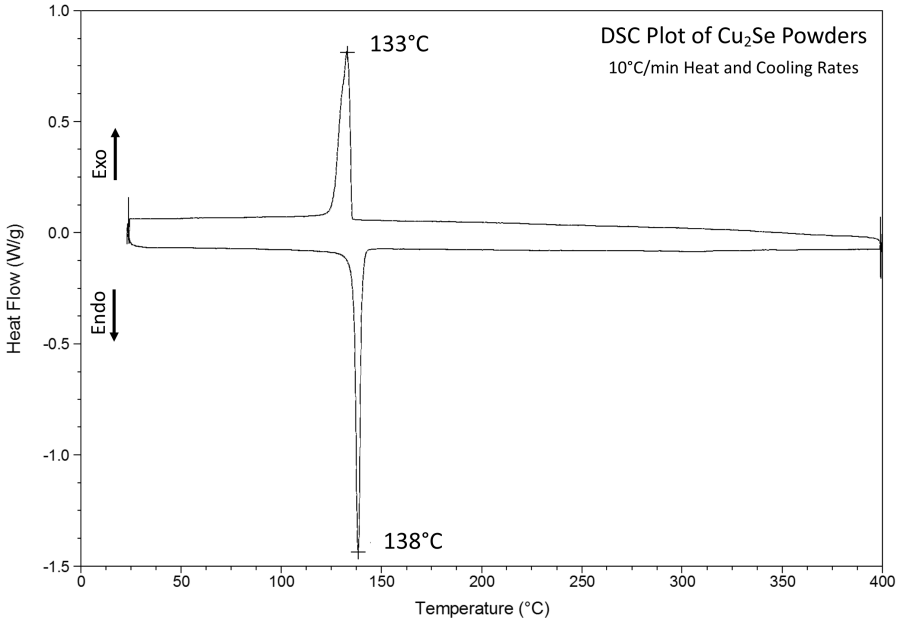

Figure 3.7: Cu_2Se DSC thermogram with indicated phase transition temperatures

DSC testing to verify the transition temperature and compare it with the theoretical values. In Figure 3.7 the sharp phase transitions happening both during cooling and heating steps are clearly visible, both their temperatures are shifted to higher values with respect to the theoretical ones, probably due to slight compositional variations. Both supercooling and superheating effects are also visible, with a transition temperature difference of 5°C from the peak detected during the heating ramp to the one belonging to the cooling ramp. Further experimentation finally conducted to the standardization of the process obtaining the procedure reported in Section 2.1.3. SEM on the

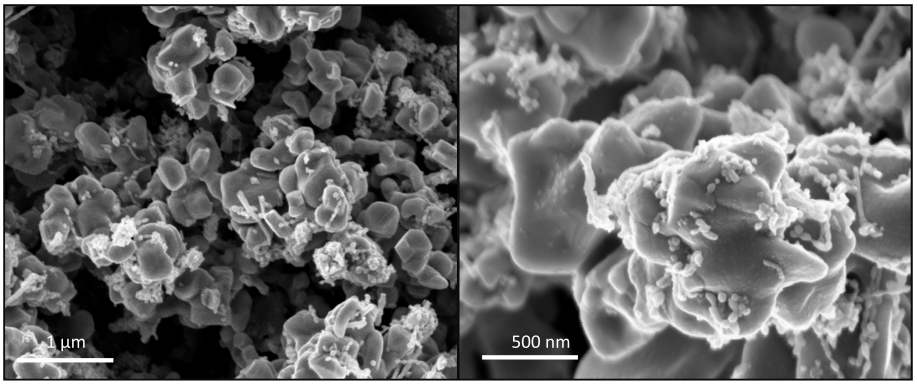

Figure 3.8: SEM micrographs of Cu_2Se sample at different magnifications

produced powders shows a larger average size with respect to the $Cu_{1.8-x}Se$ phase discussed previously, being aorund 250nm. It is interesting to notice the presence of a large amount of much smaller particles, 25-30nm, decorating the larger ones, this suggests the presence of two nucleation phases, one that takes place very early when a large majority of Copper Acetate converts to Copper Oleate and reacts with the Se-TOP and a second one that probably originates during the high temperature holding step: in these conditions further reaction of Copper Acetate is allowed and a population of very small particles is formed. While the first particles nucleated have the time to grow significantly, the growth of the second ones, created towards the end of the reaction, is stopped by the sudden lowering of the temperature at the end of the 5 minutes holding time. ICPES is performed and shows once again that copper deficiency is a characteristic of the process employed, the phase obtained is stable in the Cu_2Se crystallographic form but is more adequately described as $Cu_{2-x}Se$. Nonetheless the obtained material is believed to possess high thermoelectric performance with literature amply confirming this claim, it is therefore used as base material for the subsequent experiments.

3.2 Fabrication of Nano-Composites

As discussed in Section 1.3.4 it can be beneficial to create composites that can assign different roles to the various materials employed. Following this reasoning the idea arises of mixing the two phases that are produced in the manner previously described: Cu_2Se and $Cu_{1.8}Se$. While the first material acts as the main matrix, providing reduced lattice thermal conductivity and high thermoelectric properties, the second one becomes a carrier injector, it is in fact much richer in holes and might be able to increase the overall conductivity of the composite. The higher lattice thermal conductivity attributed to $Cu_{1.8}Se$ is believed not to be a problem in this case since, also thanks to nanostructuring, there is no direct path for phonons through a single material. Actually, it is hypothesised that the building of a two phase material can further hinder phonon motion thanks to local straining at boundaries and change in density. Finally a third effect might come into play: Energy Filtering. Thanks to a difference in the Band Gaps of the two materials electrons that pass from one to the other might be back-reflected if their energy is too low. Generally speaking this is a desirable feature in TEs since it boosts the Seebeck coefficient. It should then be possible to improve the overall thermoelectric performances both by reducing lattice thermal conductivity and improving electronic transport properties.

Two powder compositions are prepared to achieve compositing:

- Cu_2Se + 5% $Cu_{1.8}Se$
- Cu_2Se + 10% $Cu_{1.8}Se$

Both of them are defined as weight percent and are prepared by thorough mixing and grinding together the respective quantities of pure phase in an agate mortar. The mixing procedure is carried on in a glove box to limit contamination by foreign particles. The obtained powder mixes undergo X-Ray Diffraction to check detectability of the secondary phase even at this relatively low concentration, XRD patterns of composites and pure components as reference are reported in Figure 3.9. Furthermore to establish a base line also a pure $Cu_{1.8}Se$ and a pure Cu_2Se sample are prepared.

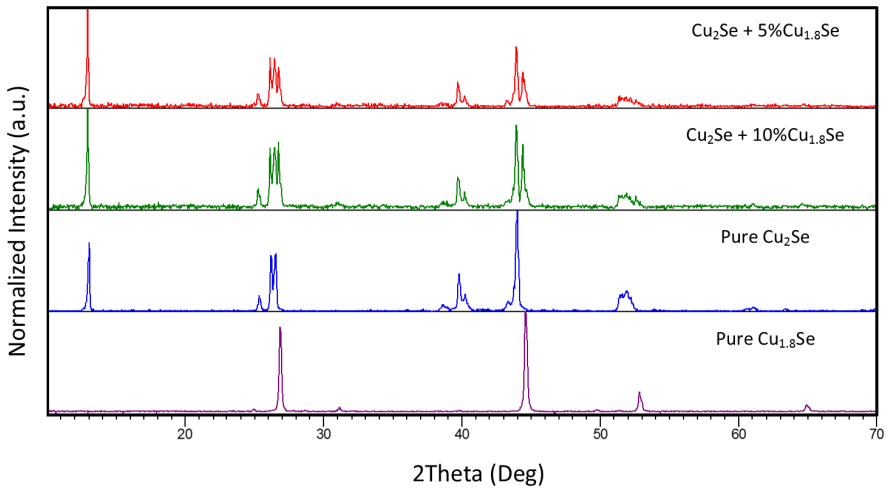

Figure 3.9: XRD patterns of Cu_2Se +5% $Cu_{1.8}Se$ powder mix, Cu_2Se +10% $Cu_{1.8}Se$ powder mix and the as produced powders of $Cu_{1.8}Se$ and Cu_2Se as reference

3.2.1 Optimization of Sintering

Depending on the compositions previously mentioned and wanted final product very diverse thermal and load histories can be applied to obtain optimal compaction. The initial conditions described are inspired by Tafti et al. work:[52] the powders are poured in a 15mm graphite die lined with graphite foil and, after insertion of the two graphite pistons in the die, a cold uniaxial pressing step is performed up to 10MPa. The specimen prepared in this way is inserted in the Spark Plasma Sintering chamber that is then kept under vacuum. The temperature is raised up to 450°C at a rate

of 50°C/min while the loading is also gradually applied topping at 75MPa uniaxial pressure. Once the final temperature is achieved a holding time of 1 min takes place. Finally, pressure is released and the die is let too cool in the chamber in vacuum. Both the short holding time and the relatively rapid cooling to room temperature are chosen to limit the grain growth of the sample. A typical compaction plot is reported in Figure 3.10.

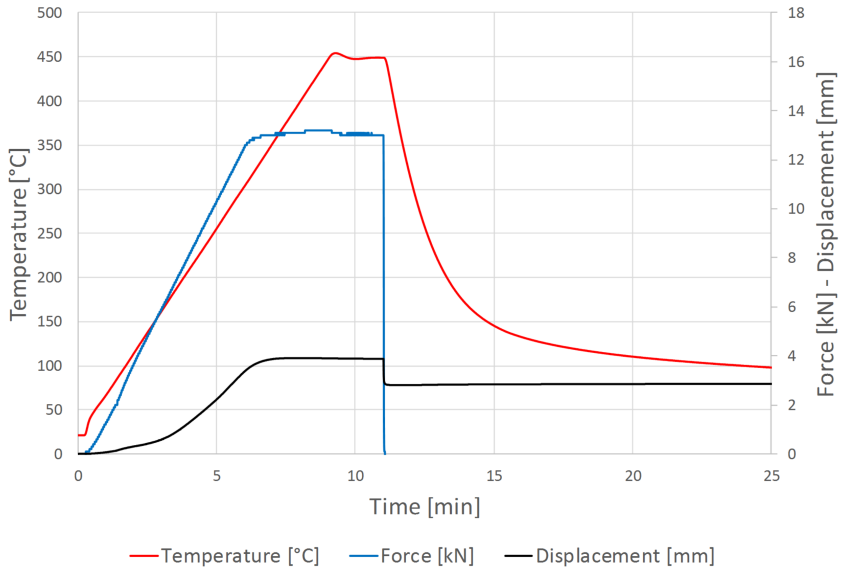

Figure 3.10: Typical compaction plot for Cu_2Se using non-optimized sintering parameters

The method reported proved successful for pure Cu_2Se allowing the production of samples with relative densities higher than 90%, as tested by Archimedes' principle. Some of the samples showed the formation of cracks, though. The mechanical failure is believed to originate from the sharp cooling rate the sample undergoes when the heating system is switched off. The fast release of the applied load is also thought to cause a sudden change in internal strains, favouring the release of internal stresses by crack formation. In order to obtain better results, a slow cooling ramp was added to the processing routine and the sintering history is tailored to each specific composition.

Cu_2Se Sintering Procedure

In order to avoid the cracking risk a cooling ramp and a slower load release are implemented in the process, also lowering the holding temperature to 400°C, while the rest of the procedure remains unchanged: the Cu_2Se pow-

ders are poured in a 15 mm die lined with graphite foil, the two graphite pistons are inserted and cold pressing at 10MPa is performed. After these steps the die is placed in the SPS machine and vacuum is created in the chamber, a temperature of 400°C is achieved at 50°C/min rate while also the loading is gradually applied up to 75MPa in the first 5 minutes. 1 minute holding follows and finally a cooling ramp begins; in 3 minutes the loading is brought to 0 and in 50 minutes the temperature is lowered to 150°C (5°C/min). At this temperature the die is left cooling naturally due to the already extremely low cooling rate. A typical compaction plot is reported in Figure 3.12, it must be noticed that the duration of the cooling ramp renders the holding at fixed temperature almost invisible on the curve. It has been found that following these steps guarantees no crack formation, allowing the release of residual stresses in the obtained samples while a high final compaction is also achieved. The sample obtained is shown in Figure 3.11 where the total absence of cracks can be verified.

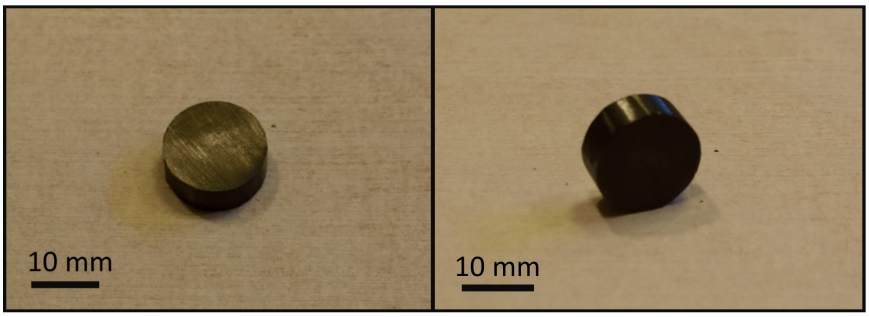

Figure 3.11: Pure Cu_2Se Sintered Pellet

$Cu_{1.8}Se$ Sintering Procedure

Multiple sintering trials testify that this phase undergoes complete compaction at much lower temperatures with respect to Cu_2Se, achieving a plateau at 280-290°C. The final procedure is thus tailored accordingly: the $Cu_{1.8}Se$ powders are poured in a 15 mm die lined with graphite foil, the two graphite pistons are inserted and cold pressing at 10MPa is performed. After these steps the die is placed in the SPS machine and vacuum is created in the chamber, a temperature of 300°C is achieved at 50°C/min rate while also the loading is gradually applied up to 75MPa. In this case no holding time follows the heating step. The sample is left cooling naturally due to the lower risk of cracking caused by lower employed temperatures. A typical compaction plot is reported in Figure 3.14. This procedure guarantees

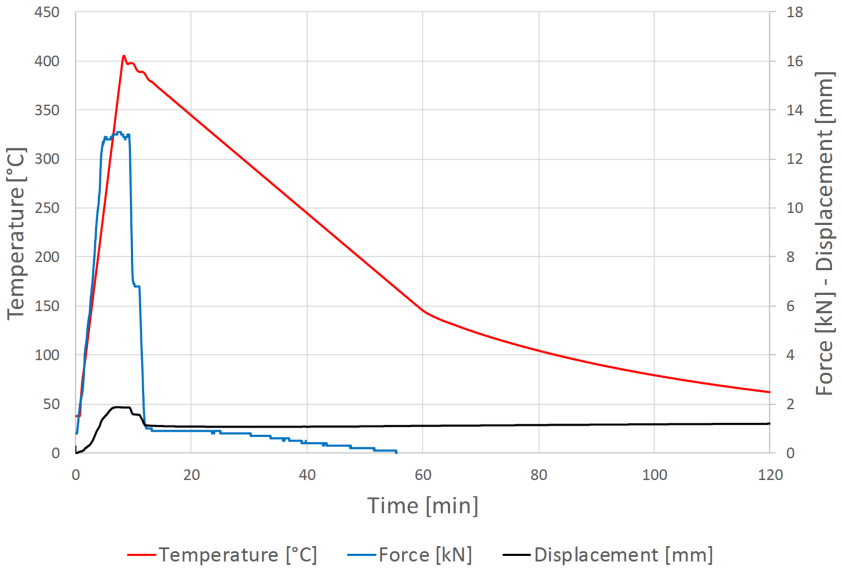

Figure 3.12: Typical compaction plot for Cu_2Se using optimized sintering parameters

both a sample with no visible cracks and good final compaction as shown in Figure 3.13.

Figure 3.13: Pure $Cu_{1.8}Se$ Sintered Pellet

Cu_2Se-$Cu_{1.8}Se$ Composites Sintering Procedure

In this case two compositions are considered: Cu_2Se + 5% $Cu_{1.8}Se$ and Cu_2Se + 10% $Cu_{1.8}Se$. Since the amount of $Cu_{1.8}Se$ phase is relatively small in both cases it was decided that a procedure similar to that employed for pure Cu_2Se should be used. After some experimentation the sintering history is optimized yielding the following steps: the powders mixtures are poured in a 15 mm die lined with graphite foil, the two graphite pistons

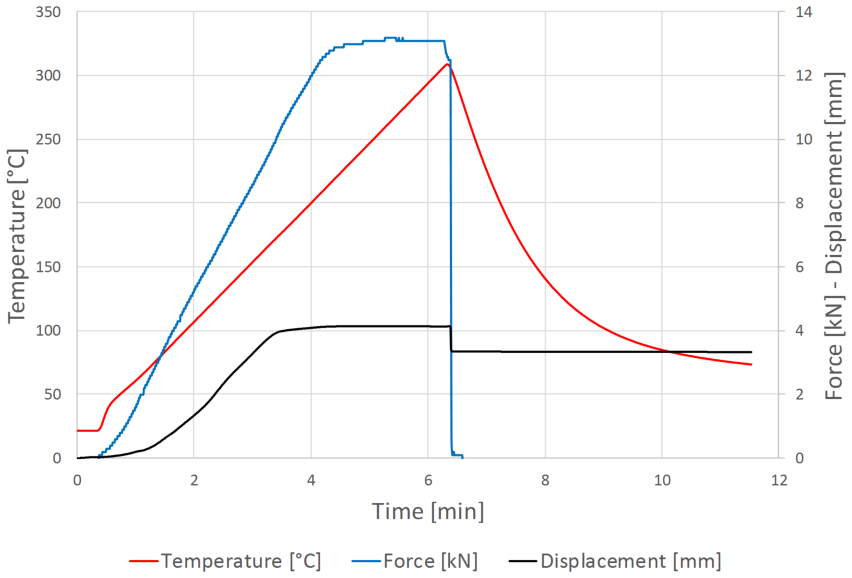

Figure 3.14: Typical compaction plot for $Cu_{1.8}Se$ using optimized sintering parameters

are inserted and cold pressing at 10MPa is performed. After these steps the die is placed in the SPS machine and vacuum is created in the chamber, a temperature of 400°C is achieved at 50°C/min rate while the loading is gradually applied up to 75MPa. 1 minute holding follows and then the specimen is unloaded and the die is left cooling. A typical compaction plot in case of 5%$Cu_{1.8}Se$ is reported in Figure 3.16, the analogous for the 10%$Cu_{1.8}Se$ is omitted since it has identical appearance. It is interesting to notice that in this case the adding of $Cu_{1.8}Se$ significantly reduces the risk of crack formation even at higher cooling rates with respect to pure Cu_2Se. This is believed to be thanks to its higher malleability with respect to the copper rich phase: during cooling and load release the softer phase can accommodate for internal stresses by plastically deforming. In Figure 3.15 it can be noticed that only a minor notch is formed on the sample while the rest of it is undamaged.

3.2.2 Structural Characterization

After sintering, the obtained pellets are tested for changes in their crystallographic structure and morphology. The first step is to check the relative density achieved, this is a good measure of how effective the compaction step is since it allows quantification of residual porosities. The density of each pellet is measured by Archimedes' principle and compared to the densities of the bulk materials taken from literature, the results are included in Table

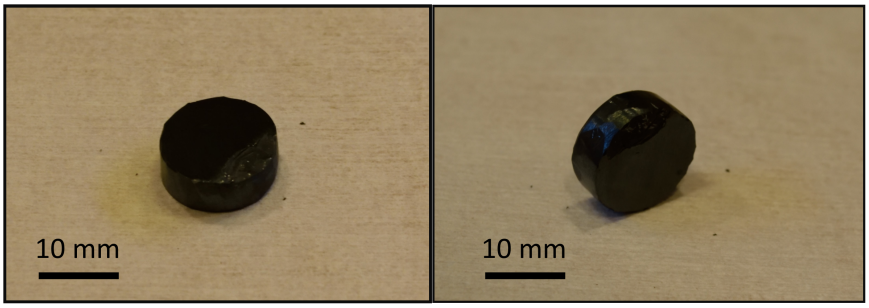

Figure 3.15: Cu_2Se and $Cu_{1.8}Se$ Composite Sintered Pellet

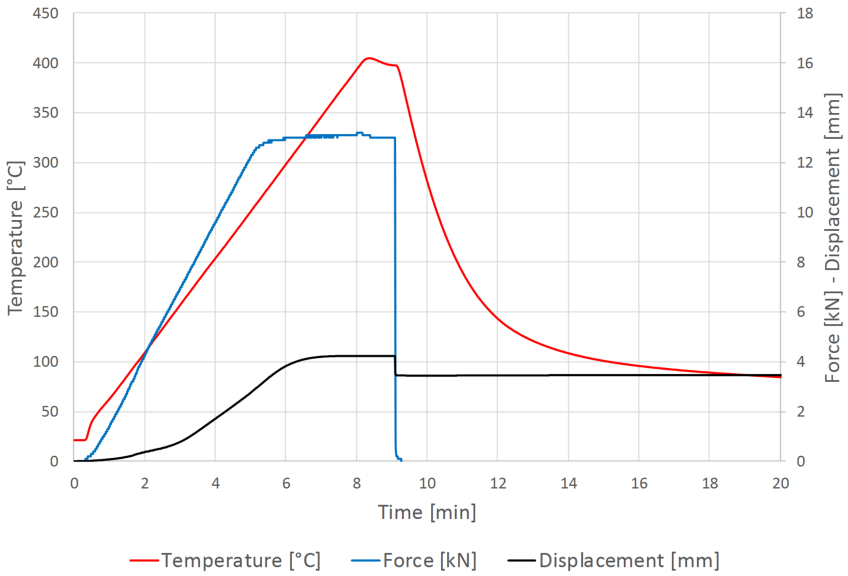

Figure 3.16: Typical compaction plot for $Cu_2Se + 5\%Cu_{1.8}Se$ using optimized sintering parameters

3.1. As can be noticed the results confirm that a satisfactory compaction is achieved, all pellets present relative densities as high or higher than 90%. This is later corroborated by the Scanning Electron Micrographs: the fracture surface appears mostly compact with very few small residual pores.

X-Ray Diffraction

The X-Ray Diffraction peaks of the samples are analysed. It is clear, by comparison with the patterns before sintering, that the various compositions behave very differently when sintered. Observing Figure 3.17, it can be immediately noticed that SPS does not visibly modify the crystal structure in the case of pure Cu_2Se, the main peaks remain unchanged while

Table 3.1: Relative Densities of Sintered Samples with respective sintering parameters

Sample	Sintering Temperature [°C]	Cooling Ramp [°C/min]	Sample Density [g/cm^3]	Relative Density
Pure Cu_2Se	400	5	6.29	0.92
Cu_2Se + 5% $Cu_{1.8}Se$	400	-	6.53	0.96
Cu_2Se + 10% $Cu_{1.8}Se$	400	-	6.51	0.95
Pure $Cu_{1.8}Se$	300	-	6.13	0.90

only a change in relative intensities is noticed. This modification is mainly attributed to the anisotropic crystalline growth that tends to strengthen certain peaks with respect to the more homogeneous powder form.

When considering the pure $Cu_{1.8}Se$, instead, extremely different phenomena take place: by comparison with the powder form new peaks arise corresponding to a completely new phase, Figure 3.18. It is then clear that $Cu_{1.8}Se$ is not left unchanged by SPS but is partially converted to a different crystallographic structure: Cu_3Se_2. This is attributed to the Copper deficiency already described in Section 3.1.3: the Cu-deficient $Cu_{1.8-x}Se$ releases its lattice distortions by the nucleation of a second phase that naturally includes less Cu. The final result is the formation of a binary system including a Cu enriched phase nearing the $Cu_{1.8}Se$ stoichiometric composition, thus gaining stability, and a Cu_3Se_2 phase that requires a lower amount of Copper to maintain its crystallographic structure.

Finally it is possible to discuss the behaviour of the Cu_2Se-$Cu_{1.8}Se$ Composites. By comparison with the XRD patterns before sintering one feature is evident, the peaks attributed to $Cu_{1.8}Se$ almost completely disappear in favour of the ones of Cu_2Se. The second noteworthy effect is the progressive shift of the peaks attributed to Cu_2Se towards larger angles when going from lower to higher $Cu_{1.8}Se$ concentrations in the composites. Both phenomena can be easily explained by Copper migration: as previously mentioned the $Cu_{1.8}Se$ phase is Copper deficient and at high temperatures it partially converts to a more stable, less distorted Cu_3Se_2. In the case of composites it is completely surrounded by Cu_2Se, though, this leads to a diffusion of Copper from one phase to the other converting part of the $Cu_{1.8-x}Se$ into $Cu_{2-x}Se$. This is clearly visible in the shift of the peaks: those of Cu_2Se progressively move to higher 2θ values, a clear indication that the unit cell volume is decreasing. When the copper ions migrate towards the more Copper deficient zones, the crystal structure compensates the increase in empty space

by crumpling and distorting, thus reducing the average unit cell volume. On the other hand it would be theoretically possible to witness a peak shift towards lower 2θ values for the leftover $Cu_{1.8}Se$, this unfortunately is not possible since its signal is under the XRD detection limit. All these observations can be verified by looking at Figure 3.19 and its zoomed-up version Figure 3.20 where the reported features are highlighted.

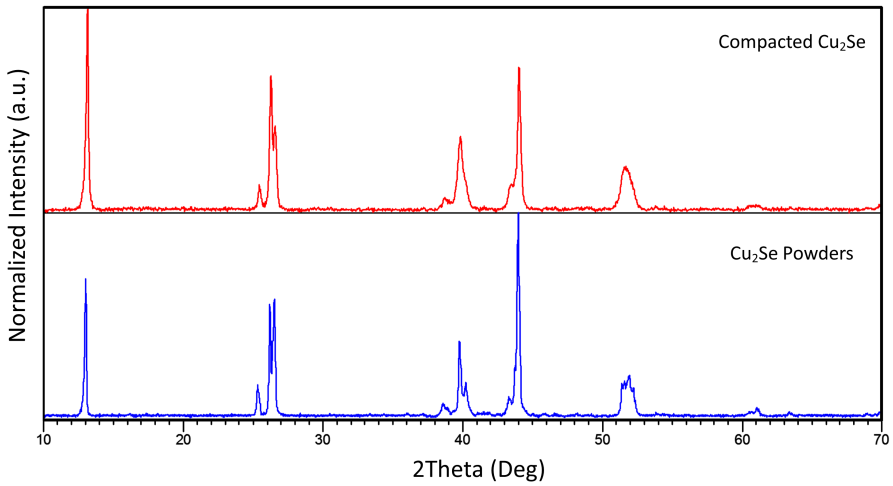

Figure 3.17: XRD patterns of compacted Cu_2Se compared to Cu_2Se powders as produced

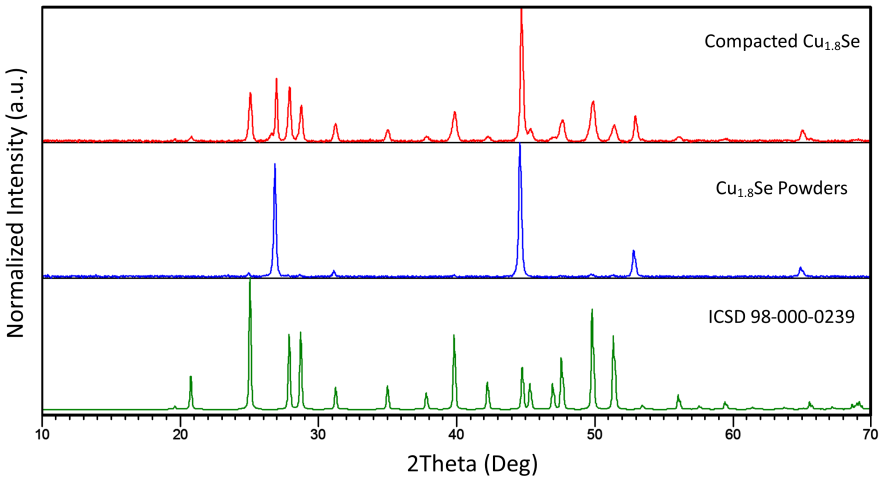

Figure 3.18: XRD patterns of $Cu_{1.8}Se$ compacted sample, $Cu_{1.8}Se$ powders as produced and ICSD 98-000-0239 Reference Pattern for Cu_3Se_2

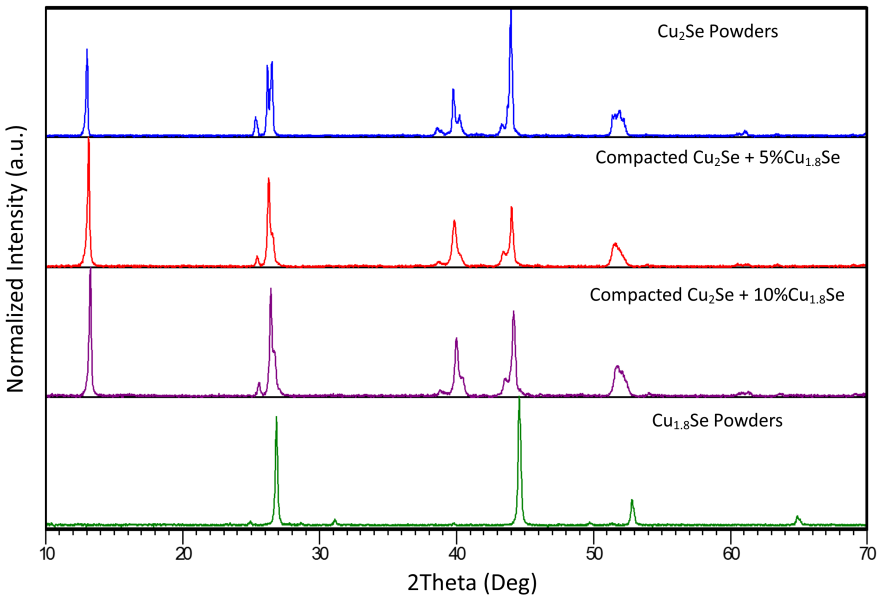

Figure 3.19: XRD patterns of Cu_2Se powders as produced, Cu_2Se +5% $Cu_{1.8}Se$ compacted sample, Cu_2Se +10% $Cu_{1.8}Se$ compacted sample and $Cu_{1.8}Se$ powders as produced

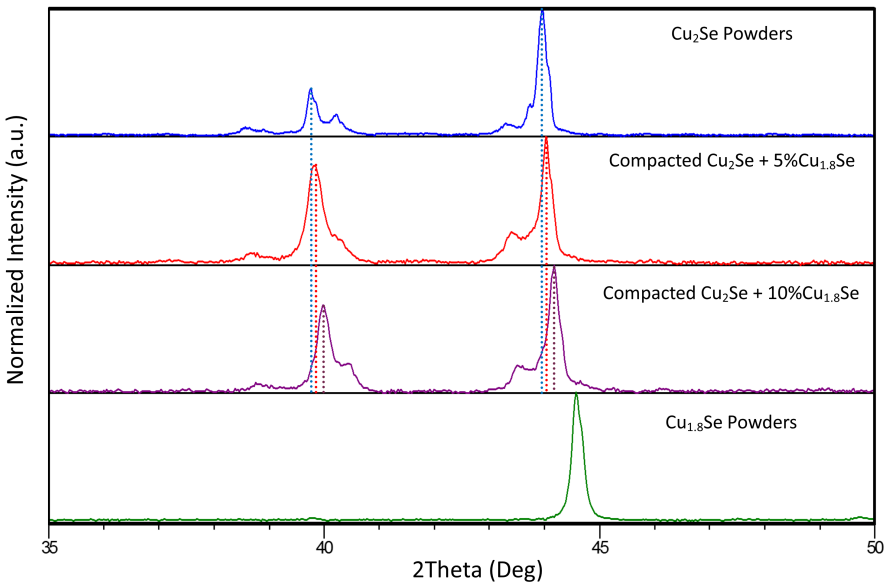

Figure 3.20: Highlight of peak shift in XRD patterns of Cu_2Se powders as produced, Cu_2Se +5% $Cu_{1.8}Se$ compacted sample, Cu_2Se +10% $Cu_{1.8}Se$ compacted sample and $Cu_{1.8}Se$ powders as produced

Scanning Electron Microscopy

As anticipated Scanning Electron Microscopy is also performed on the samples, part of them are broken off and the fracture surface is then studied. In case of Cu_2Se the surface appears compact with small amounts of residual pores. The fracture happens mainly by cleavage of the grains testifying that the sintering step allows the formation of strong interconnections between the particles of powder. As it is possible to observe in Figure 3.21, the grain size is slightly increased from the 250nm of the as prepared powders to an average of 300nm and minor pores are visible on some of the cleaved surfaces. These openings have diameters ranging in size from 15nm to 35nm and are not considered an issue for the mechanical and transport properties of the material. The sample is also checked by EDX for elemental homogeneity, demonstrating that no evident segregation of metallic Copper or Selenium takes place: the corresponding micrograph and mappings are reported in Figure 3.22.

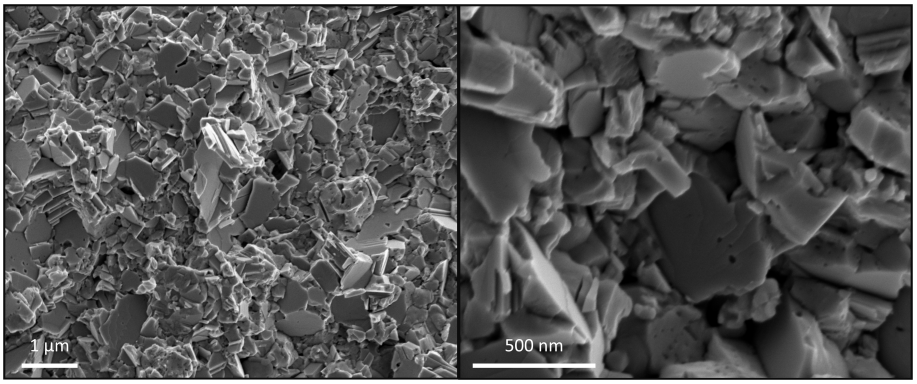

Figure 3.21: SEM micrographs of Cu_2Se compacted sample at different magnifications

When considering $Cu_{1.8}Se$, instead, the surface appears less compact and the presence of crack lines at grain boundaries can be noticed. The fracture happens by a mixture of cleavage of the grains and grain boundary separation. The grain size increase is much more significantly with respect to the one seen for the Cu_2Se sample, the average passes from the 60nm of the as produced powders to around 200nm. This is believed to be the effect of the easy migration of ions taking place in this material, effect that also allows the nucleation of the previously mentioned Cu_3Se_2 secondary phase. Also higher presence of small pores can be noticed, with diameters between 15 and 35 nm they account for the lower relative density measured with respect to the Cu_2Se sintered sample. The elemental homogeneity is also checked by EDX, demonstrating that no evident segregation of metallic Copper or Selenium

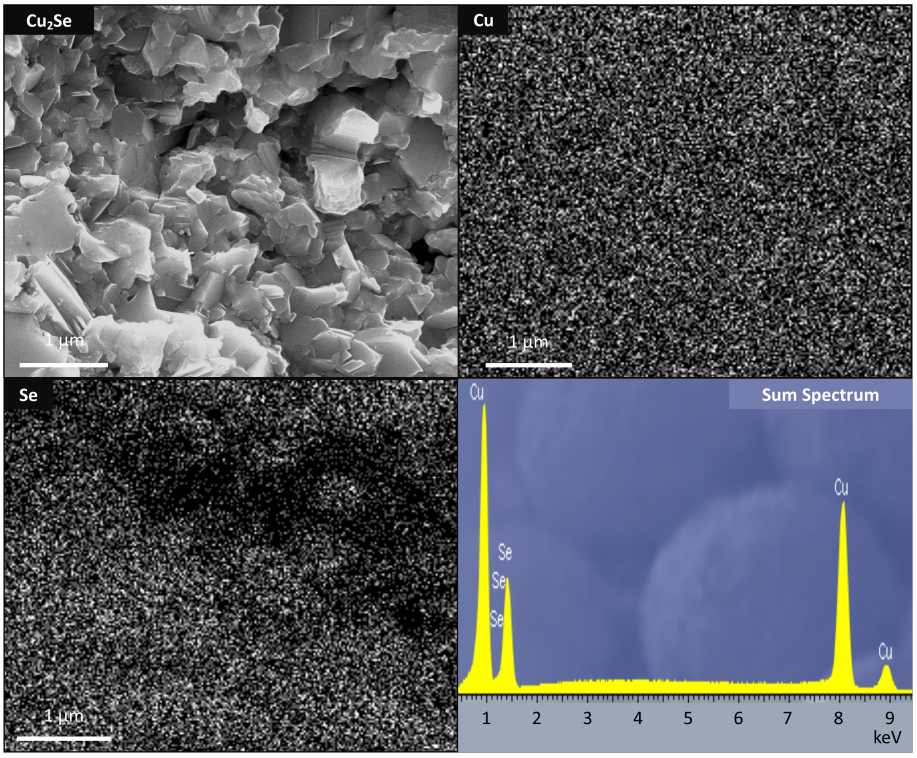

Figure 3.22: Energy Dispersive X-Ray Spectrometry: SEM micrograph of Cu_2Se compacted sample with Cu and Se mappings

takes place: the corresponding micrograph and mappings are reported in Figure 3.24.

Finally the two composite compacted samples are analysed side-by-side to allow a comparison between lower and higher $Cu_{1.8}Se$ concentration. In both cases the fracture surfaces appear compact and with a reduced amount of pores. The fracture happens by cleavage of the grains, once again testifying that the sintering process allows the formation of robust bonds between the particles of powder. When it comes to grain size a slight difference is present between the two samples: Cu_2Se +5%$Cu_{1.8}Se$ presents an average of 250 nm while Cu_2Se +10%$Cu_{1.8}Se$ is around 220nm. These values arise from the different concentrations of $Cu_{1.8}Se$ that, as previously shown, has a lower dimensionality with respect to Cu_2Se. In both samples it is possible to distinguish two kinds of particles: the smaller ones originated from the $Cu_{1.8}Se$ phase and the large ones coming from the growth of Cu_2Se grains, the origin of the two sizes is confirmed by the higher count of small particles in the second sample with respect to the first one. Finally a very small amount of pores can be observed and the few present have larger dimen-

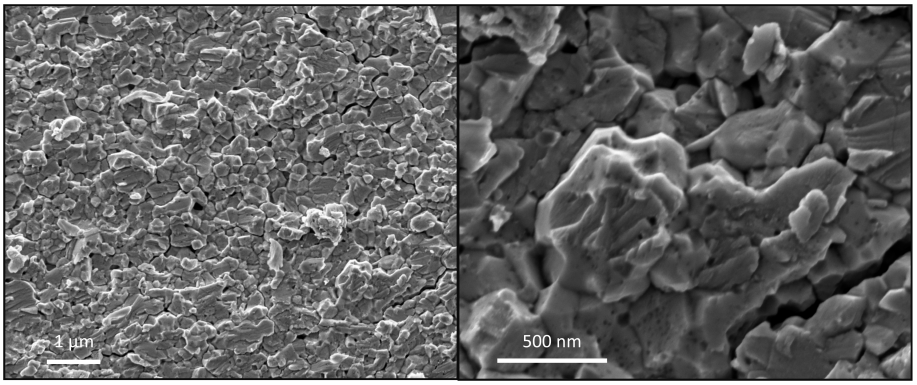

Figure 3.23: SEM micrographs of $Cu_{1.8}Se$ compacted sample at different magnifications

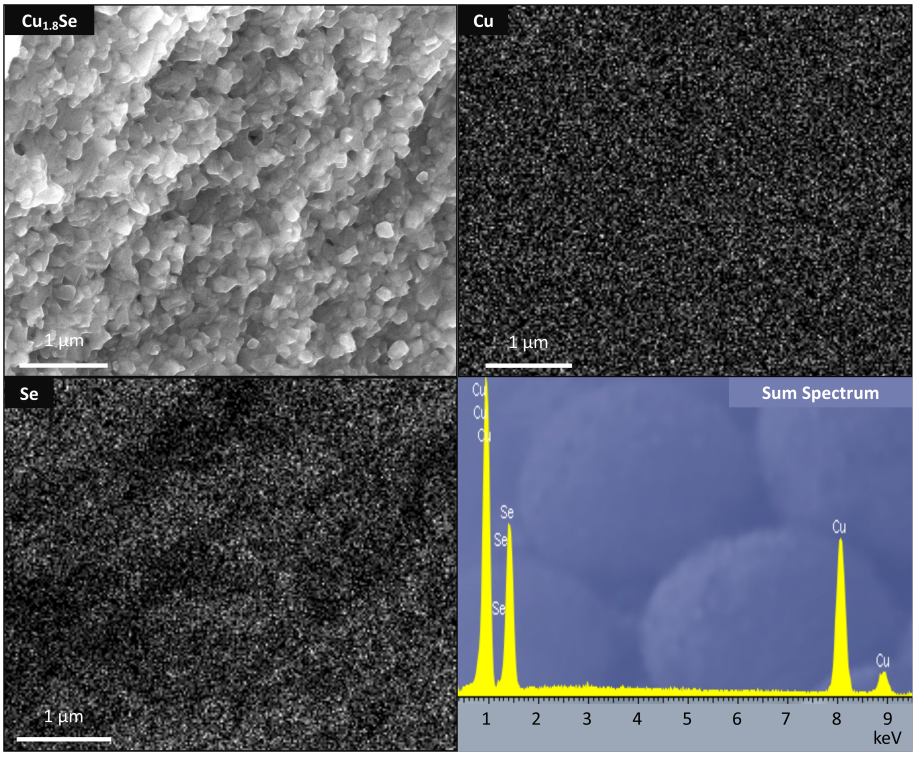

Figure 3.24: Energy Dispersive X-Ray Spectrometry: SEM micrograph of $Cu_{1.8}Se$ compacted sample with Cu and Se mappings

sions with respect to the ones in pure Cu_2Se compacted samples, ranging from 25 to 50nm. The samples are also checked by EDX for elemental homogeneity, demonstrating that no evident segregation of metallic Copper or Selenium takes place, the corresponding micrograph and mappings are reported in Figure 3.26 and Figure 3.27. Overall, all the samples show satisfactory morphology with the conservation of nano-sized features and valid levels of compaction, with no evident faults or undesirable modifications of their structures. A summary of the main results coming from SEM and EDX characterization is reported in Table 3.2

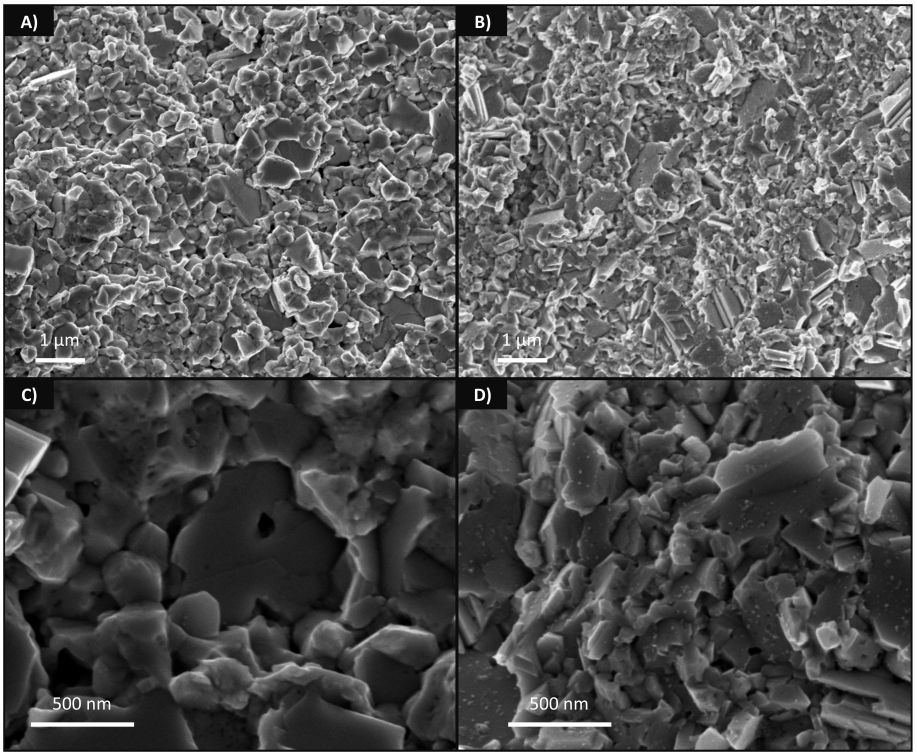

Figure 3.25: SEM micrographs at different magnifications: A),C)Cu_2Se +5%$Cu_{1.8}Se$ compacted sample, B),D)Cu_2Se +10%$Cu_{1.8}Se$ compacted sample

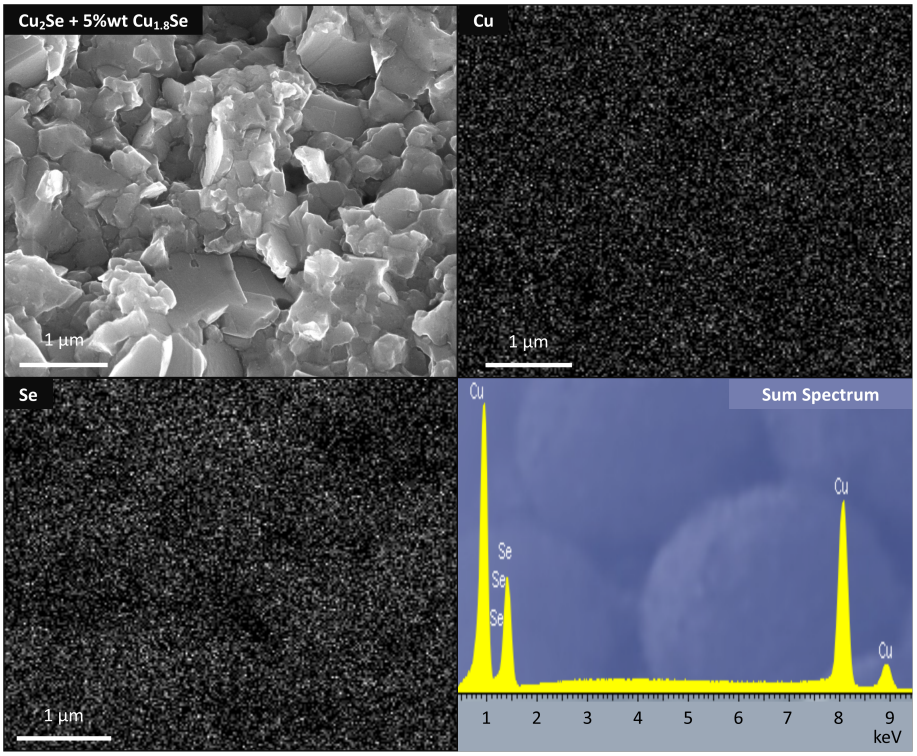

Figure 3.26: Energy Dispersive X-Ray Spectrometry: SEM micrograph of Cu_2Se +5%$Cu_{1.8}Se$ compacted sample with Cu and Se mappings

Table 3.2: Summary Table of EDX and SEM characterization techniques

Sample	Average Grain Size [nm]	Pores Diameter [nm]	Fracture Type	EDX Cu/Se Ratio
Pure Cu_2Se	300	15-35	Cleavage	1.91
Cu_2Se + 5% $Cu_{1.8}Se$	250	25-50	Cleavage	1.90
Cu_2Se + 10% $Cu_{1.8}Se$	220	25-50	Cleavage	1.88
Pure $Cu_{1.8}Se$	300	15-35	Cleavage/Grain Separation	1.72

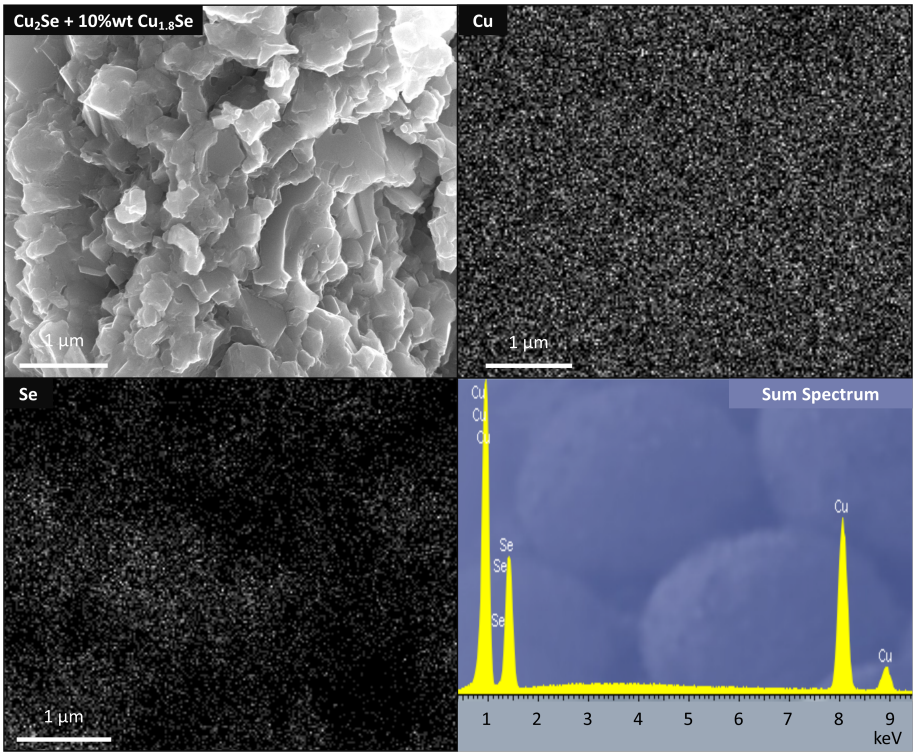

Figure 3.27: Energy Dispersive X-Ray Spectrometry: SEM micrograph of Cu_2Se +10%$Cu_{1.8}Se$ compacted sample with Cu and Se mappings

3.2.3 Transport Characterization

As stated in Section 2.3.6 the samples are sent to Technical University of Denmark (DTU) for transport properties measurements. Unfortunately, to date, the results regarding thermal conductivity have not been received, this limits the estimation to the electronic transport properties and considerations on zT coefficient and efficiency will be attached as a separate appendix as soon as possible. Nonetheless it is interesting to compare the available results starting from the electrical conductivity: as predicted this is extremely high for $Cu_{1.8}Se$ and it decreases progressively going from the pure phase to the composites containing higher amounts of Cu_2Se, reaching relatively low values for this last pure phase. These results show how compositing strongly influences electronic transport and it is believed that a very significant increase in carrier concentration takes place when the secondary phase is added. A more accurate observation reveals that the conductivity at high temperatures is almost doubled from the pure Cu_2Se to the 5%wt composite and more than doubles again from it to the 10%wt. The effect is even more dramatic at lower temperatures and these improvements are regarded as very relevant particularly considering the relatively small amount of secondary phase added.

The next step is studying the effects that compositing has on the Seebeck coefficient. Previously it was hypothesized that it could be improved by the presence of a secondary phase acting as energy filtering barrier, unfortunately this is not the case as clearly visible in Figure 3.29. There is a clear trend that can be explained by the semi-metallic properties of $Cu_{1.8}Se$: this material has very low Seebeck coefficient and when added to the matrix of Cu_2Se it tends to lower the overall potential difference generated. This results in a progressive decrease of Seebeck values going from the pure Cu_2Se phase to the higher concentrations of $Cu_{1.8}Se$.

The two opposing trends identified have a marked effect on the Power Factor (PF). This term is used to estimate the power that can be extracted from a TE material at a given temperature and also corresponds to a part of the numerator of the zT coefficient defined in Section 1.3.3:

$$PF = \sigma \cdot S^2 \tag{3.4}$$

The PF curves clearly show that while the value rapidly saturates for pure Cu_2Se and the 5%wt composite, the %10wt composite has an ongoing improvement of the value up to the end of the measurement at 600°C, the same tendency exhibited by $Cu_{1.8}Se$. This trend is attributed to the presence of $Cu_{1.8}Se$ that is able to compensate the low Seebeck coefficient by strongly

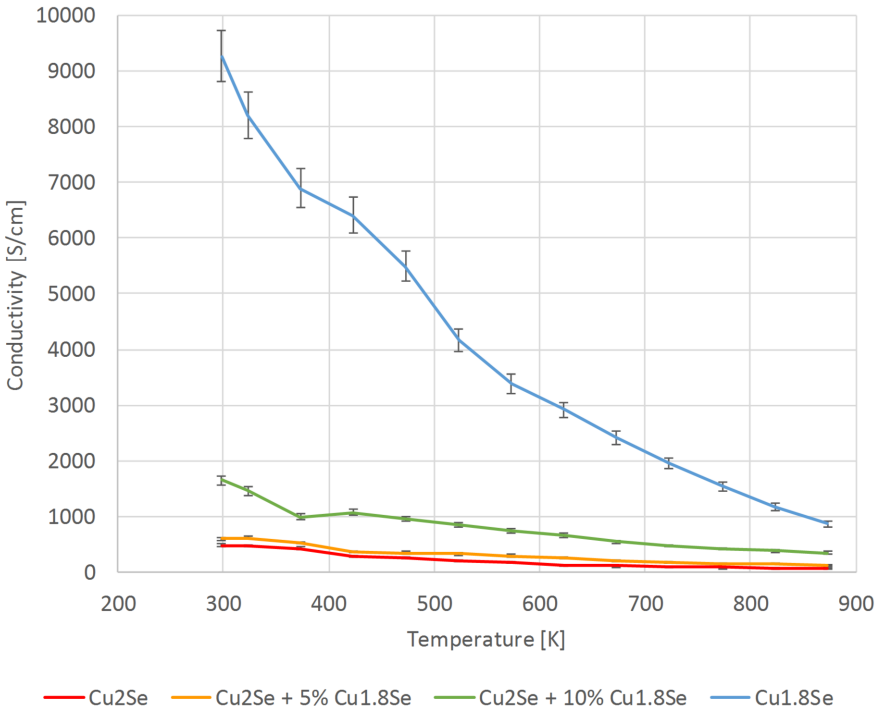

Figure 3.28: Comparison of the Conductivity of the different materials

limiting the electrical resistivity increase. It is also interesting to notice the strong deviations in the PF registered both for pure Cu_2Se and for the 5%wt composite, these are believed to be the result of the transition of Cu_2Se from its α to its β phase, these in fact start taking place around the 100°C as already shown by the DSC results. $Cu_{1.8}Se$ on the other hand does not undergo a phase transition and its curve does not present any peak, this is also reflected in the 10%wt composite for which the sudden change in electronic properties is not detected. Overall the composite including 10% by weight of $Cu_{1.8}Se$ in a Cu_2Se matrix has the highest PF over most of the temperature range measured, demonstrating that its value can be maximized by a proper compromise between Seebeck coefficient and electrical conductivity. Unfortunately no considerations on the zT coefficients are possible with the present data but it is hoped that the thermal conductivity is not significantly increased by the presence of $Cu_{1.8}Se$, thus allowing to have an overall increase of the coefficient of merit, boosting the conversion efficiency of the material.

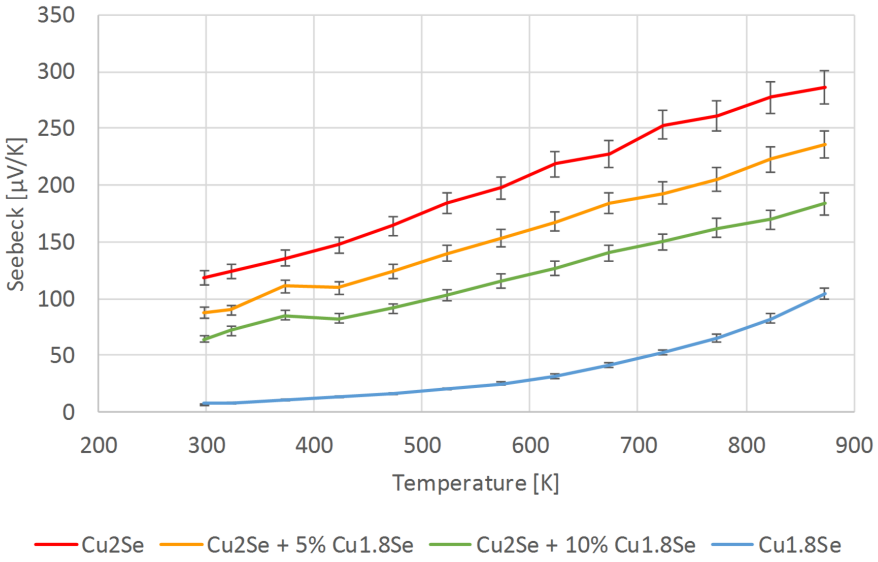

Figure 3.29: Comparison of the Seebeck coefficients of the different materials

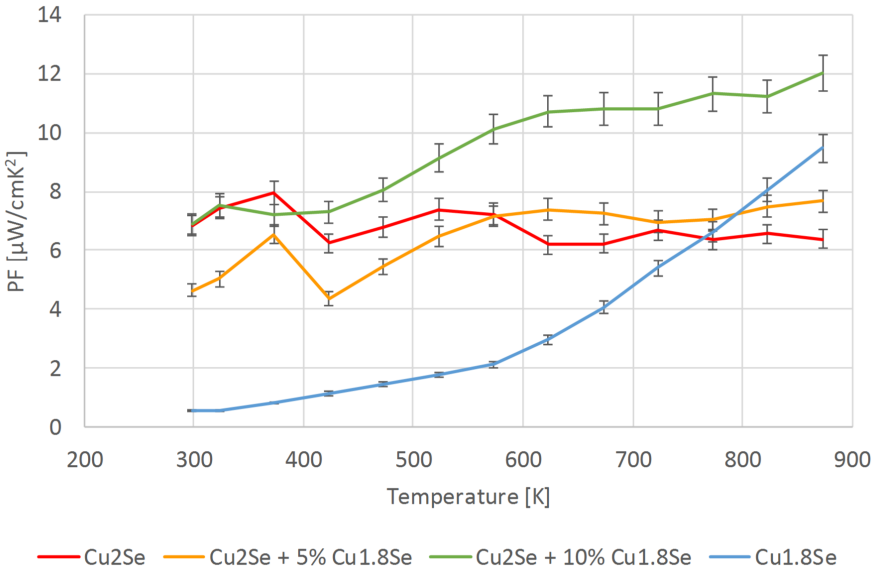

Figure 3.30: Comparison of the PFs of the different materials

Chapter 4

Conclusions

Using microwave assisted thermolysis a fast, reproducible and energetically advantageous synthesis route for Copper Selenides has been obtained. Compared to other studies it has been possible to isolate two related phases following specific reaction processes. While many papers do not distinguish between the Cu_2Se and the $Cu_{1.8}Se$ phases, reporting them as a single material, in this work it has been demonstrated that the two exist as separate entities and chemical synthesis routes can be tuned to obtain specifically one of the two if desired. This has opened the route for the production of materials that present a well-defined percentage of one phase over the other. The as produced powders range in size from an average of 60nm for $Cu_{1.8}Se$ to 250nm for Cu_2Se, they are therefore highly suitable for the production of bulk nanostructured themoelectric materials, possibly yielding high phonon scattering and reducing thermal conductivity. The approach utilized is furthermore believed to show great promise for low energy consumption and industrial scalability.

Sintering processes have been optimized for the different compositions of powders produced. It has been demonstrated that the dispersion of $Cu_{1.8}Se$ in Cu_2Se not only does not negatively affect the final compaction parameters of the samples but apparently improves them, yielding higher relative densities and an overall less brittle material. This is believed to be the result of higher malleability of the $Cu_{1.8}Se$ phase during the cooling step. Furthermore the parameters employed limit the grain growth during sintering of Cu_2Se with samples showing a 20% increase of their average grain size.

Finally the analysis of the electronic properties of the obtained single-phase materials and composites gives interesting perspective on the interaction of the two phases. It is demonstrated that significant increase in the PF can be achieved when the right amount of secondary phase is added to

bulk Cu_2Se. The trends show, in fact, that the strong decrease of Seebeck coefficient, caused by the presence of $Cu_{1.8}Se$, is compensated by the extreme reduction in electrical resistivity of the composite. It is concluded that among the specimens tested the Cu_2Se + 10%wt $Cu_{1.8}Se$ has the best compromise between electrical conductivity and Seebeck coefficient maximizing PF.

All things considered, these results are an interesting step for the future development of better thermoelectric materials: both microwave synthesis and spark plasma sintering are techniques that can be scaled up for industrial manufacturing and their inherently bottom up nature allows production with significantly lower processing energy requirements while still achieving substantial rates and highly tunable final products. In particular for medium-high temperatures applications, Copper Selenides are considered a promising candidate and this work is meant to be a contribution to their better understanding and development, in the belief that the production of themoelectric power modules for everyday applications is now not far-off in the future.

Chapter 5

Future Work

It has been demonstrated that microwave assisted thermolysis is a valid production route for $Cu_{2-x}Se$ phases, allowing the obtainment of nanopowders of high purity and with good dimensional control. The same technique could be applied to other interesting thermoelectric materials such as Tin Selenides, Copper Tellurides or doped Copper Selenides: these families could benefit from a novel approach to their synthesis but optimization of reaction parameters is needed. A more thorough study on microwave synthesis mechanisms could also allow for extension of the technique to many different material classes without the need for trial and error tuning procedures. Furthermore, exploring possible alternatives to Trioctylphosphine would increase the green aspect of the synthetic route chosen, eliminating the last expensive and relatively hazardous component of the whole process.

Further studies on the effect of the $Cu_{1.8}Se$ phase in the Cu_2Se matrix are needed to better correlate how transport and thermoelectric properties scale with its volume fraction. The same thinking also goes in further investigating the effects of sintering on the grain size and phase distribution of the composites and pure samples.

The nanocompositing has also been shown to be a valid addition to nanostructuring and Spark Plasma Sintering, with its flexibility, can be tailored to the compaction of composites with very diverse compositions. This encourages further experimentation with materials coupling, possible options being: Thermoelectric Material-Metal composites to improve electrical performance or Thermoelectric Material-Ceramic composite to enhance mechanical stability and possibly further reduce lattice thermal conductivity.

Finally a very interesting possibility would be pushing the limits of microwave synthesis by producing ordered composites like core-shell structures and nanowires, these have been shown to improve thermoelectric perfor-

mance in other studies and, if a straightforward process could be developed their use in commercial products would rapidly become possible.

Bibliography

[1] T. Akao, Y. Tarui, T. Onda, and Z. C. Chen. Fabrication of Zn4Sb3 bulk thermoelectric materials reinforced with SiC whiskers. *Journal of Electronic Materials*, 43(6):2047–2052, 2014.

[2] B. Alexandrov, K. Z. Ahmed, and S. Mukhopadhyay. An on-chip autonomous thermoelectric energy management system for energy-efficient active cooling. *Proceedings of the 2014 International Symposium on Low Power Electronics and Design*, 1:51–56, 2014.

[3] G. Bale. CdZnTe Radiation Detectors for Hard X-ray Astronomy. *Doctoral Thesis University of Leicester, UMI Nr U535327*, University, 2001.

[4] N. P. Blake, S. Latturner, J. D. Bryan, G. D. Stucky, and H. Metiu. Band structures and thermoelectric properties of the clathrates Ba8Ga16Ge30, Sr8Ga16Ge30, Ba8Ga16Si30, and Ba8In16Sn30. *The Journal of Chemical Physics*, 115(17):8060, 2001.

[5] BMW. BMW Vision Efficient Dynamics. *Munich Motorshow*, 2009.

[6] T. D. Krauss C. M. Evans, M. E. Evans. Mysteries of TOP-Se Revealed: Insights into Quantum Dot Nucleation. *NIH Public Access*, 4(164):10973–10975, 2011.

[7] D. J. Chakrabarti and D. E. Laughlin. The Cu-Se (Copper-Selenium) system. *Bulletin of Alloy Phase Diagrams*, 2(3):305–315, 1981.

[8] J. H. Choi and Y. K. Han. Structural, electronic, and optical properties of bulk Cu2Se. *Current Applied Physics*, 15(11):1417–1420, 2015.

[9] J. Cui, X. Zhang, Y. Li, and Y. Gao. Effect of band gap reduction on the thermoelectric properties of In2Se3 based semiconductors after co-doping of Cu and Te. *Xiyou Jinshu Cailiao Yu Gongcheng/Rare Metal Materials and Engineering*, 41(12):2118–2122, 2012.

[10] J. M. Cullen and J. M. Allwood. The efficient use of energy: Tracing the global flow of energy from fuel to service. *Energy Policy*, 38(1):75–81, 2010.

[11] A. De Gloria. *Applications in Electronics Pervading Industry, Environment and Society*, volume 351. 2014.

[12] G. Dennler, R. Chmielowski, S. Jacob, F. Capet, P. Roussel, S. Zastrow, K. Nielsch, I. Opahle, and G. K. H. Madsen. Are binary copper sulfides/selenides really new and promising thermoelectric materials? *Advanced Energy Materials*, 4(9):1–12, 2014.

[13] M. S. Dresselhaus, G. Chen, M. Y. Tang, R. Yang, H. Lee, D. Wang, Z. Ren, J. P. Fleurial, and P. Gogna. New directions for low-dimensional thermoelectric materials. *Advanced Materials*, 19(8):1043–1053, 2007.

[14] C. F. Cooper E. Hermite. GB patent 2836, 1901.

[15] F. El Akkad, B. Mansour, and T. Hendeya. Electrical and Thermoelectric Properties of Cu2Se and Cu2S. *Materials Research Bulletin*, 16:535–539, 1981.

[16] F. Gascoin, S. Ottensmann, D. Stark, S. M. Haile, and G. J. Snyder. Zintl phases as thermoelectric materials: Tuned transport properties of the compounds CaxYb1-xZn2Sb2. *Advanced Functional Materials*, 15(11):1860–1864, 2005.

[17] Y. Gelbstein, J. Davidow, E. Leshem, O. Pinshow, and S. Moisa. Significant lattice thermal conductivity reduction following phase separation of the highly efficient GexPb1- xTe thermoelectric alloys. *Physica Status Solidi (B)*, 7(7):n/a–n/a, 2014.

[18] L. Gulay, M. Daszkiewicz, O. Strok, and A. Pietraszko. Crystal structure of Cu2Se. *Chemistry of Metals and Alloys*, 4(2011):200–205, 2011.

[19] G. M. Guttmann, D. Dadon, and Y. Gelbstein. Electronic tuning of the transport properties of off-stoichiometric PbxSn1-xTe thermoelectric alloys by Bi2Te3 doping. *Journal of Applied Physics*, 118(6):065102, 2015.

[20] E. F. Hampl. US patent 3853632, 1974.

[21] T. Haruyama. Performance of Peltier elements as a cryogenic heat flux sensor at temperatures down to 60 K. *Cryogenics*, 41(5-6):335–339, 2001.

[22] J. P. Heremans, V. Jovovic, E. S. Toberer, A. Saramat, K. Kurosaki, A. Charoenphakdee, S. Yamanaka, and G. J. Snyder. Enhancement of Thermoelectric Efficiency in PbTe by Distortion of the Electronic Density of States. *Science*, 321(5888):554–557, 2008.

[23] Intel Corporation. CPU Power Density. In *Intel Development Forum*, 2004.

[24] J. W. Jiang, H. S. Park, and T. Rabczuk. Molecular dynamics simulations of single-layer molybdenum disulphide (MoS2): Stillinger-Weber parametrization, mechanical properties, and thermal conductivity. *Journal of Applied Physics*, 114(6), 2013.

[25] K. Koumoto and I. Terasaki. Complex Oxide Materials for Thermoelectric Applications. *Materials Research Society Bulletin*, 31:206–210, 2006.

[26] A. I. Krivchikov, V. G. Manzhelii, O. A. Korolyuk, B. Y. Gorodilov, and O. Romantsova. Thermal conductivity of tetrahydrofuran hydrate. *Physical Chemistry Chemical Physics*, 7(5):728–30, 2005.

[27] K. Kurosaki, A. Kosuga, H. Muta, M. Uno, and S. Yamanaka. Ag9TlTe5: A high-performance thermoelectric bulk material with extremely low thermal conductivity. *Applied Physics Letters*, 87(6):23–26, 2005.

[28] V. L. Kuznetsov, L. A. Kuznetsova, and D. M. Rowe. Effect of partial void filling on the transport properties of NdxCo4Sb12 skutterudites. *Journal of Physics: Condensed Matter*, 15(29):5035–5048, 2003.

[29] E. Lee, J. Ko, J. Kim, W. Seo, S. Choi, K. Lee, W. Shim, and W. Lee. Enhanced thermoelectric properties of Au nanodot-included Bi2Te3 nanotube composites. *Journal of Mater Chemistry C*, 4(6):1313–1319, 2016.

[30] F.S. Liu, M.J. Huang, Z.N. Gong, W.Q. Ao, Y. Li, and J.Q. Li. Enhancing the thermoelectric performance of β-Cu2Se by incorporating SnSe. *Journal of Alloys and Compounds*, 651:648–654, 2015.

[31] H. Liu, X. Shi, F. Xu, L. Zhang, W. Zhang, L. Chen, Q. Li, C. Uher, T. Day, and G. J. Snyder. Copper ion liquid-like thermoelectrics. *Nature Materials*, 11(5):422–425, 2012.

[32] LLLN. Estimated USA Energy Consumption in 2014. *Laboratory Livermore Lawrence National -WEB-669625*, 2014.

[33] K. Mohseni. Effective Cooling of Integrated Circuits Using Liquid Alloy Electrowetting Kamran Mohseni Department of Aerospace Engineering Sciences. *Engineering Sciences*, 2005.

[34] C. B. Murray, and C. R. Kagan, and M. G. Bawendi. Synthesis and Characterization of Monodisperse Nanocrystals and Close-Packed Nanocrystal Assemblies. *Annual Review of Materials Science*, 30(1):545–610, 2000.

[35] D. Narducci, E. Selezneva, G. Cerofolini, S. Frabboni, and G. Ottaviani. Impact of energy filtering and carrier localization on the thermoelectric properties of granular semiconductors. *Journal of Solid State Chemistry*, 193:19–25, 2012.

[36] G. S. Nolas, J. Poon, and M. Kanatzidis. Recent Developments in Bulk Thermoelectric Materials. *Materials Research Society Bulletin*, 31(03):199–205, 2006.

[37] Y. Z. Pei, L. D. Chen, W. Zhang, X. Shi, S. Q. Bai, X. Y. Zhao, Z. G. Mei, and X. Y. Li. Synthesis and thermoelectric properties of KyCo4Sb12. *Applied Physics Letters*, 89(22), 2006.

[38] B. Poudel, Q. Hao, Y. Ma, Y. Lan, A. Minnich, B. Yu, X. Yan, D. Wang, A. Muto, D. Vashaee, X. Chen, J. Liu, M. S. Dresselhaus, G. Chen, and Z. Ren. High-Thermoelectric Performance of Nanostructured Bismuth Antimony Telluride Bulk Alloys. *Science*, 320(5876):634–638, 2008.

[39] S. B. Riffat and X. Ma. Thermoelectrics: A review of present and potential applications. *Applied Thermal Engineering*, 23(8):913–935, 2003.

[40] M. Romdhane, C. Gourdon, and G. Casamatta. Development of a thermoelectric sensor for ultrasonic intensity measurement. *Ultrasonics*, 33(2):139–146, 1995.

[41] B. C. Sales, D. Mandrus, and R. K. Williams. Filled skutterudite antimonides: A new class of thermoelectric materials. *Science*, 272(5266):1325, 1996.

[42] A. Saramat, G. Svensson, A. E. C. Palmqvist, C. Stiewe, E. Mueller, D. Platzek, S. G. K. Williams, D. M. Rowe, J. D. Bryan, and G. D. Stucky. Large thermoelectric figure of merit at high temperature in Czochralski-grown clathrate Ba8Ga16Ge30. *Journal of Applied Physics*, 99(2), 2006.

[43] J. Schilz, M. Riffel, K. Pixius, and H. J. Meyer. Synthesis of thermoelectric materials by mechanical alloying in planetary ball mills. *Powder Technology*, 105(1-3):149–154, 1999.

[44] G. J. Snyder and E. S. Toberer. Complex thermoelectric materials. *Nature materials*, 7(2):105–114, 2008.

[45] A. Soni, Y. Shen, M. Yin, Y. Zhao, L. Yu, X. Hu, Z. Dong, K. A. Khor, M. S. Dresselhaus, and Q. Xiong. Interface Driven Energy Filtering of Thermoelectric Power in Spark Plasma Sintered Bi2Te2.7Se0.3 Nanoplatelet Composites. *Nano Letters*, 2012.

[46] University of Cambridge. Introduction to thermal and electrical conductivity. *Dissemination of IT for the Promotion of Materials Science*, 2013.

[47] O. Vancauwenberghe, J. Short, E. Giehler, P. Bidlstein, P. Ancey, and M. Gschwind. Microsensor for the preventive detection of water condensation: operating principle and interface electronics. *Sensors and Actuators A*, 53:304–308, 1996.

[48] C. B. Vining. An inconvenient truth about thermoelectrics. *Nature materials*, 8(2):83–85, 2009.

[49] B. Wölfing, C. Kloc, J. Teubner, and E. Bucher. High performance thermoelectric Tl9BiTe6 with an extremely low thermal conductivity. *Physical Review Letters*, 86(19):4350–4353, 2001.

[50] D. A. Wright. Thermoelectric Properties of Bismuth Telluride and its Alloys. *Nature*, 181(4612):834, 1958.

[51] X.Shi. Phase transition and high temperature thermoelectric properties of copper selenide Cu2-xSe (0<x<0.25). *Chinese Physics B*, 20(8):87201, 2011.

[52] M. Yakhshi Tafti. Microwave Assisted Organometallic Synthesis, Structural Characterization and ThermoelectricEvaluation of Cu2Se. *Doctoral Thesis KTH, Diva2:925901*, 2016.

[53] J. Yang and F. R. Stabler. Automotive applications of thermoelectric materials. *Journal of Electronic Materials*, 38(7):1245–1251, 2009.

[54] T. Yao. Thermal properties of AlAs/GaAs superlattices. *Applied Physics Letters*, 51(22), 1987.

[55] K. Yazawa, M. Hao, B. Wu, A. K. Silaen, C. Q. Zhou, T. S. Fisher, and A. Shakouri. Thermoelectric topping cycles for power plants to eliminate cooling water consumption. *Energy Conversion and Management*, 84:244–252, 2014.

[56] K. Yazawa, Y. R. Koh, and A. Shakouri. Optimization of thermoelectric topping combined steam turbine cycles for energy economy. *Applied Energy*, 109:1–9, 2013.

[57] L. Zou, B. Zhang, Z. Ge, and L. Zhang. Enhancing thermoelectric properties of Cu 1.8+xSe compounds. *Journal of Materials Research*, pages 1047–1053, 2014.

[58] T. H. Zou, X. Y. Qin, D. Li, B. J. Ren, G. L. Sun, Y. C. Dou, Y. Y. Li, L. L. Li, J. Zhang, and H. X. Xin. Enhanced thermoelectric performance via carrier energy filtering effect in Zn4Sb3 alloy bulk embedded with (Bi 2Te3)0.2(Sb2Te3)0.8. *Journal of Applied Physics*, 115(5):0–4, 2014.